CytoMAP: a spatial analysis toolbox reveals features of myeloid cell organization in lymphoid tissues

Caleb R Stoltzfus[1], Jakub Filipek[1], Benjamin H Gern[2,3], Brandy E Olin[1], Joseph M Leal[1], Miranda R Lyons-Cohen[1], Jessica Huang[1], Clarissa L Paz-Stoltzfus[4], Courtney R Plumlee[2], Thomas Pöschinger[5], Kevin B Urdahl[2,1], Mario Perro[6], Michael Y Gerner[1]

1: University of Washington, Department of Immunology, Campus Box 358059, 750 Republican Street, Seattle, WA 98109, USA Phone: 206-685-3610, gernermy@uw.edu
2: Seattle Children's Research Institute, Seattle, WA, 98109, USA
3: Department of Pediatrics, University of Washington, Seattle, WA, 98195, USA
4: School of Medicine, University of Washington, Seattle, WA, 98195, USA
5: Roche Innovation Center Munich, Pharmaceutical Research & Early Development (pRED), Discovery Pharmacology, Nonnenwald 2, 82377 Penzberg, Germany
6: Roche Innovation Center Zurich, Pharmaceutical Research & Early Development (pRED), Wagistrasse 10, 8952 Schlieren, Switzerland

ABSTRACT

Recently developed approaches for highly-multiplexed 2-dimensional (2D) and 3D imaging have revealed complex patterns of cellular positioning and cell-cell interactions with important roles in both cellular and tissue level physiology. However, robust and accessible tools to quantitatively study cellular patterning and tissue architecture are currently lacking. Here, we developed a spatial analysis toolbox, Histo-Cytometric Multidimensional Analysis Pipeline (CytoMAP), which incorporates neural network based data clustering, positional correlation, dimensionality reduction, and 2D/3D region reconstruction to identify localized cellular networks and reveal fundamental features of tissue organization. We apply CytoMAP to study the microanatomy of innate immune subsets in murine lymph nodes (LNs) and reveal mutually exclusive segregation of migratory dendritic cells (DCs), regionalized compartmentalization of SIRPa$^-$ dermal DCs, as well as preferential association of resident DCs with select LN vasculature. These studies describe DC organization in LNs, and provide a comprehensive analytics toolbox for in-depth exploration of quantitative imaging datasets.

INTRODUCTION

Appropriate organization of cells within tissues shapes both cellular and organ level physiology, and is involved in major pathological conditions, such as infections, autoimmunity, and cancer. For the immune system in particular, recent advances in intravital microscopy and multiplexed imaging approaches have revealed that the spatial organization of innate and adaptive immune cell populations in lymphoid tissues is highly complex and intimately involved in promoting immune homeostasis, as well as in the efficient generation of protective responses during infection or after vaccination.[1–3] As an example, different subsets of dendritic cells (DCs), innate antigen presenting cells responsible for eliciting T cell responses, localize to distinct regions within lymph nodes (LNs) in a highly organized and non-uniform fashion.[4–7] Spatial segregation of these functionally distinct DC subsets directly influences the sensitivity, kinetics, magnitude, and quality of T cell responses, thus playing a critical role in the generation of adaptive immunity.[5,8,9] Notably, these findings have only recently been observed in what were previously considered to be relatively well-studied organs, suggesting that high-dimensional imaging approaches can yield important new insights into how complex biological systems operate.

This need to map the precise location and molecular properties of cells in tissues has inspired a number of emerging methods for highly multiplexed in situ cellular profiling (e.g. histo-cytometry, CODEX, MIBI, STARMAP).[4,10–17] These techniques generate panoptic datasets describing phenotypic, transcriptional, functional, and morphologic cellular properties, while retaining information on the precise 2-dimensional (2D) or 3D positioning of cells within tissues, thus potentiating a more complete understanding of cellular function directly in situ. Analysis of images generated by these methods requires multiple processing steps, including image pre-processing, cell segmentation, object classification, and spatial analysis.[18–20] Existing platforms excel at different steps of this pipeline. For image segmentation and pre-processing, there are several commercial and open source software packages capable of defining cellular boundaries within 2D, and 3D multi-channel imaging datasets.[18,21] For spatial analysis, existing advanced software or published code include statistical tools for defining cellular phenotypes, as well as use nearest-neighbor algorithms to identify preferential interactions among different cell types.[10,11,19,22–24] Nevertheless, there is a lack of accessible and simple to use informatics tools for extracting quantitative and comprehensible information on the complex spatial relationships between different cell types and their microenvironments, as well as for revealing the fundamental organizational features of complex tissues, especially for large volumetric and whole slide datasets. This has hampered the ability of biologists with access to high-dimensional imaging technologies to obtain an in-depth understanding of the spatial relationships of cells and localized microenvironments within their datasets and limited the utility of these advanced imaging approaches.

Here, we developed a user-friendly, spatial analysis toolbox, Histo-Cytometric Multidimensional Analysis Pipeline (CytoMAP), which incorporates diverse statistical approaches for extracting and quantifying information about cellular spatial positioning and cell-cell interactions across tissues. CytoMAP is specifically designed to analyze datasets generated with existing quantitative imaging approaches, which already incorporate information on cell phenotype, morphology, and location. CytoMAP simplifies analysis of cell positioning and tissue

architecture by grouping cells into spatial neighborhoods. These neighborhoods are explored in detail using established and newly-developed statistical and visualization modules, including: machine learning based data clustering, cellular position correlation, distance analysis, tissue structure visualization through dimensionality reduction, network mapping, and 2D or 3D region reconstruction. CytoMAP analysis reveals and quantitates 2D or 3D tissue architecture, local cell composition and cell-cell spatial networks, as well as the spatial interconnectedness of tissue microenvironments. CytoMAP also facilitates robust sample-to-sample comparison, allowing exploration of structural and compositional heterogeneity across samples and diverse experimental conditions. Furthermore, CytoMAP can, in principle, be utilized for analysis of positionally-resolved data generated with diverse in situ cellular profiling methods, allowing integration of this analytical toolbox into various disciplines.

We validate and demonstrate the capabilities and utility of CytoMAP by investigating innate and adaptive cell organization in well-characterized, steady state murine LNs. Our analyses recapitulate previous descriptions of the cellular microenvironments within these tissues, as well as identify novel features of myeloid cell organization in LNs. Specifically, CytoMAP analysis reveals preferential positioning of migratory SIRPa$^-$ dermal DCs (dDCs) within the lower cortical ridge bordering the LN medulla.[25,26] Furthermore, 3D spatial analysis with CytoMAP reveals preferential association of LN-resident DCs with LN blood vessels, which supports the established role of DCs in functional maintenance of high endothelial venules[27,28], as well as indicates that these anatomical structures could provide guidance cues to regulate DC localization in LNs. We also find that individual vascular networks in LNs are composed of unique regions associated with distinct DC subsets, indicating that LN vasculature may be heterogeneous based on the local interacting cell partners.[29,30] Finally, we demonstrate the ability of CytoMAP to define microenvironments in complex disease associated tissues, including solid tumors and *Mycobacterium tuberculosis* (Mtb) infected murine lung granulomas.[31–34] Together, these data indicate that CytoMAP is a versatile and powerful tool for in-depth exploration of cellular positioning and tissue architecture.

RESULTS

CytoMAP enables analysis of tissue microenvironments, cellular interactions, and tissue structure

The conceptual basis for the spatial analysis used in CytoMAP centers on the notion of tissues being composed of cells that group together to form local microenvironments or neighborhoods (Fig. 1a). These neighborhoods can incorporate one or several different cell types and can extend across large distances to generate tissue regions, which coalesce further to form the overarching tissue structure. The goal of CytoMAP is to utilize cell phenotype and positioning information, as generated by existing methods (e.g. histo-cytometry), to reveal how cells are distributed within tissues, how they generate different local microenvironments, and how the organization of local microenvironments leads to the generation of global tissue structure. The basic CytoMAP workflow and available analytical tools are presented in Fig. 1. For the tissues analyzed here, multi-parameter confocal microscopy and histo-cytometry were used to quantify the spatial location of immune cell subsets.[4,13,35] In principle, datasets with spatially resolved quantitative

features at any length scale (e.g. intracellular molecular organization, cellular positioning in tissues, human demographic data) and generated by any high-parameter approach could be investigated with CytoMAP. In this specific analysis application, the acquired phenotypic properties and positional information of individual cell objects are passed to CytoMAP, which spatially subdivides the cells into local neighborhoods of user-defined dimensions (Fig. 1b). The size of the neighborhood depends on the granularity of the desired information, with larger neighborhood size revealing more global patterns within the tissue, and smaller neighborhoods providing fine-grained information on hyperlocal cellular composition and tissue structure. If the dataset provided has no thickness, or thickness less than the user defined radius, CytoMAP utilizes a cylindrical (thin section 3D data) or circular (2D data) neighborhood window, otherwise a spherical neighborhood will be used. The generated neighborhoods contain information on the cell composition, density, expression of specific molecules, as well as data on any additional structural or functional parameters (e.g. local density of collagen fibers as detected by additional probes). These parameters are passed to a self-organizing map (SOM) that clusters the neighborhoods. The SOM is a neural network based clustering algorithm, which organizes information topologically, allowing extraction and quantification of critical features and unique tissue regions within highly complex datasets.[36–39] This algorithm groups neighborhoods with similar cellular composition into clusters, defined here as tissue "regions", which are denoted by the different colors in the top of the example heatmap in Fig. 1b. This heatmap allows direct visualization of the cellular composition of the neighborhoods (columns on the heatmap) in the identified regions, as well as shows the relative prevalence of the different regions within the imaged sample, as denoted by the size of the region color bars. Given that the individual neighborhoods contain positional information (x,y,z) from the raster scan, they can be spatially remapped, as well as demarcated using the region color code. This allows direct visualization of the size and structure of the different regions within the tissue (Fig. 1b).

CytoMAP has many additional built-in features to visualize and quantify the spatial properties of cells, neighborhoods, and regions within imaged tissues and across multiple samples (Fig. 1c). In particular, local cell density within individual neighborhoods can be used to correlate the location of different cell types, revealing which cell populations preferentially associate with one another, or conversely avoid one another. This correlation analysis can be performed across multiple samples, and can be done either over entire tissues or within specified tissue regions. This is important, as region specific spatial correlations may reveal different cellular relationships in tissues with varied cell-cell associations across different tissue compartments. Distances of cells with respect to borders of tissue regions can also be easily evaluated (Fig. 1c), which may provide information on the relative infiltration of cells into specific tissue compartments (e.g. T cell infiltration into tumors). Additionally, dimensionality reduction algorithms can be used to visualize tissue structure and complexity, as well as for sample-to-sample comparison. In particular, a new visualization approach, Pseudo-space, as well as a previously established spatial t-distributed Stochastic Neighbor Embedding (t-SNE) analysis both reduce the complexity and heterogeneity of neighborhood cell composition into one- or two-dimensional plots, respectively (Fig. 1c).[40] This helps reveal the fundamental relationships of cells with one another (Pseudo-space), as well as facilitates comparison of the neighborhood heterogeneity within or across multiple samples (spatial t-SNE). These dimensionality reduction

techniques also help reveal how the tissue neighborhoods are organized to generate global tissue structure, which can be further quantified using region interaction network mapping (Fig. 1c) that calculates which regions preferentially border one another within the samples. Finally, CytoMAP allows comparison of region prevalence across different replicates or treatment conditions, which is a notoriously difficult task for heterogeneous samples with complex tissue architecture (Fig. 1c). Thus, the combination of analytical tools built directly into CytoMAP allows the user to explore spatially resolved data from an individual cell's length scale up to whole tissues, or across cohort studies.

CytoMAP quantifies well-defined tissue structure in LNs

We first validated the CytoMAP workflow by analyzing murine LN tissues, which have well-defined organization of basic immune cell types.[2] To accomplish this, a 20μm thick section of a draining LN from a C57BL/6 immunized mouse was stained with a panel of directly conjugated antibodies against distinct innate and adaptive immune populations and imaged using a confocal microscope. The image in Fig. 2a shows staining of the tissue with markers for B cells (B220), DCs (CD11c), and T cells (CD3), demonstrating pronounced segregation of these cell types to previously defined tissue compartments.[2] Individual cells within the image were next segmented in 3D, and the mean fluorescent intensity (MFI), as well as the (x,y,z) positioning of the resulting cell objects were imported into FlowJo for hierarchical gating of three primary cell types: T cells, B cells, and CD11c-expressing cells, which are mainly DCs (Fig. 2b), as described previously.[4,13,35] Next, the positional data on these cell populations were imported into CytoMAP for further processing. In CytoMAP the cells were subdivided into 30μm radius neighborhoods using the *Raster Scan Neighborhoods* function, which digitally raster scanned a cylindrical window with the user-defined radius over the dataset (Fig. 2c). This neighborhood radius size was chosen empirically, as it provided an optimal balance of spatial granularity and processing speed to reveal fundamental features of cellular organization for this specific sample, and was consistent with biological data on the dispersion distances of secreted cytokines.[41] A SOM was next used to cluster these neighborhoods based on the cellular composition (number of cells in a neighborhood divided by the total number of cells in that neighborhood), but not utilizing the positional information of the neighborhoods within tissues. Exclusion of the positions of the neighborhoods allows for comparison of compositionally similar, but spatially distal neighborhood types. Given that the number of regions used for SOM clustering requires user input and thus can be subjected to bias, we incorporated statistical tools to determine the optimal number of regions needed to reveal the underlying data structure. In this example, the number of regions was determined using the Davies-Bouldin criterion, which uses the ratio of within-cluster to between-cluster distances.[42,43] The heatmap in Fig. 2d shows the cell composition (rows) of the individual neighborhoods (columns) and which cluster/region they were assigned to (top color bar). This analysis identified different tissue regions that were primarily composed of either B cells, T cells, DCs, or those with mixed cellular composition. These regions were next visualized by plotting the positions of the color-coded neighborhoods (Fig. 2e). This plot demonstrates reconstruction of the original image, with unbiased identification of different tissue compartments, including the B cell follicles (blue), the deep T cell zone (red), the outer T zone

paracortex and the T-B border (orange), as well as the LN medullary and subcapsular regions (green). Of note, the red/orange regions at the top of the reconstructed image (Fig. 2e) correspond to noise in the original confocal image (Fig. S1a). In computationally heavy image processing pipelines, special care must be taken to either accurately remove such artifacts or to ensure appropriate interpretation of the results.

In addition to discreet region definitions, we implemented a novel dimensionality reduction data visualization function, *Pseudo-space*, to visualize the continuous region transitions within tissues, and investigate how cells are distributed across different tissue compartments (Fig. 2f). Pseudo-space allows the user to sort the neighborhoods by the absolute number or composition of different cell types within the neighborhoods and plots the neighborhoods in this sorted order on a linear Pseudo-space axis. This provides a qualitative picture of how different cell types change in their composition across the neighborhoods along this user defined dimension. For the LN analysis, the neighborhoods were sorted such that B cell rich neighborhoods fell to the left and T cell rich neighborhoods fell to the right along the Pseudo-space axis. Cellular composition of the neighborhoods was then normalized and smoothed along the Pseudo-space axis, aiding the visualization of cell populations with different tissue abundance and with substantial heterogeneity across the tissue. Pseudo-space visualization demonstrated that as the percentage of B cells in the neighborhoods declined, the percentage of T cells increased (Fig. 2f), mirroring what was observed in the original image (Fig. 2a). In the transitional area between the B cell and T cell rich neighborhoods, Pseudo-space analysis revealed an increased portion of DCs, which likely corresponds to the increased abundance of DCs in the medullary and paracortical regions of the LN. Thus, Pseudo-space provides the user with a way to reduce the complexity of tissue structure to a single dimension, aiding in visualization of cellular relationships within complex tissues and linearizing complex microenvironments.

In addition to manual dimensionality reduction, we implemented t-SNE dimensionality reduction to explore the neighborhood heterogeneity based on cellular composition and biomarker expression on a two-dimensional plot (Figs. 2g, 2h, S2b). Again, positional information of the neighborhoods was explicitly not used for the t-SNE analysis. This revealed complex structure in the LN dataset with clearly demarcated, but also interconnected clusters of neighborhoods within the t-SNE 2D space (Fig. 2g). Color-coding of neighborhoods based on region clustering, as defined in Fig. 2d, revealed clear association of the distinct regions with the different clusters generated by the t-SNE analysis, suggesting that both methods are capable of identifying cellular organization within tissues. This was confirmed using manual gating, directly within the t-SNE plot (Fig. 2i), and spatial mapping (Fig. 2j) of the t-SNE clusters, which accurately reconstructed the global tissue architecture, as well as clearly identified image artifacts (black color-coded gate Fig. 2i-j). t-SNE analysis also demonstrated the inter-connected nature of the regions, with the neighborhood regions assigned to the B cell follicle and T cell zone regions being connected with one another by neighborhoods assigned to the paracortical region (orange, Fig. 2g). This is likely due, in part, to smoothing effects from raster scanning the neighborhoods in steps of half the defined radius, such that neighborhoods partially overlap. However, this t-SNE data structure also captures features of the actual tissue organization, identifying the paracortical T-B border regions where T cells and B cells are in sufficient spatial

proximity to be included in the same neighborhood (N2, Fig. 2c). It is likely that lowering the radius scan size would reduce but not eliminate the interconnectedness of these regions, as even in tissues with extremely sharp compartment boundaries, individual cells would still exhibit differential neighboring partners at the border vs. the center of that compartment. Thus, the t-SNE analysis is able to reveal features of tissue organization based on neighborhood cell composition without being provided information on the positioning of that neighborhood within the sample.

To further explore the overarching tissue structure, we next implemented network analysis to interrogate the interconnectedness of the different regions with one another by calculating the percentage of the region borders that are shared with other regions (Fig. S1c). Mapping of these bordering relationships revealed that the T cell zone regions (red) were connected to the B cell regions (blue) via the paracortical regions (orange), thus directly recapitulating the t-SNE analysis and the original image (Fig. S1c, 2a, 2g). Together, these proof-of-concept data indicate that the CytoMAP analysis tools were capable of robustly identifying the key features of cellular organization and tissue structure for relatively simple cell types with well-characterized spatial properties.

Myeloid cell organization in steady state LNs

To test the performance of CytoMAP on datasets with more complex cellular organization, we next turned to investigating the localization of different myeloid cell subsets in steady state LNs, as these cell populations have been previously shown to display intricate, non-overlapping distribution patterns within these tissues.[2–5] To this end, 20μm sections from steady state LNs were stained with a 12-plex antibody panel to detect distinct DC and macrophage subsets, as well as to visualize T cells, B cells, and different blood and lymphatic stromal cells as reference structural markers. As above, tissues were imaged (Fig. 3a) and distinct cell populations were identified by histo-cytometry (Fig. 3b, S2a). Positional and MFI data on these cell types were next passed to CytoMAP for analysis. Basic spatial remapping of these populations in CytoMAP recapitulated the general LN structure, as well as qualitatively validated previous findings on the location of different DC and macrophage subsets (Fig. 3c). In particular, we observed that subcapsular sinus (SCS) and medullary (Med) macrophages localized to the outer LN periphery and medullary regions, respectively. Resident cDC1 and cDC2 populations also exhibited previously established spatial patterns, with the resident cDC2s preferentially localizing in peripheral LN regions, and the resident cDC1s more evenly distributed across the LN parenchyma and within the T cell zone (Fig. 3c, S2b).[4,7,44] Similarly, visualization of the migratory DC subsets confirmed previous observations, with $CD207^+$ cells (Langerhans cells and migratory cDC1s) located within the central T cell zone, and the $CD301b^+$ and $SIRPa^+$ dermal DC (dDC) subsets located in regions bordering the B cell follicles and in the lower cortical ridge, respectively (Fig. 3c, S2b).[4,6,7,45,46] In addition, histo-cytometry analysis revealed a recently described population of migratory $SIRPa^-$ dDCs, although the spatial positioning of this population has not been established in these previous studies.[25,26] Qualitative visualization of this migratory DC subset revealed that these cells were predominantly localized in the lower cortical ridge bordering the LN medulla (Fig. 3c, S2b). Visual inspection of the original confocal data

confirmed abundant presence of SIRPa$^-$ migratory dDCs in this LN compartment, with these cells forming a dense cuff-like cellular aggregate at the border of the T cell zone and the LN medulla (Fig. 3a).

CytoMAP was next used to quantify features of cellular organization within these steady state LNs. To aid in accurate classification of the tissue regions, additional spot objects were generated based on different landmark channels demarcating known LN structures (i.e. CD3, B220, and Lyve1 for the T cell zone, B cell follicles and lymphatic vessels, respectively), and the positional data from these landmark objects were also passed into CytoMAP. In addition, using the *Generate Random Points* function in CytoMAP, a population of randomly distributed points (RDP) were defined throughout the LN and were used to compare to the distribution of the imaged cells (Fig. S2b). As above, the cells and landmark spots were subdivided into individual neighborhoods by digitally raster scanning a 30μm radius neighborhood filter using the *Raster Scan Neighborhoods* function. These neighborhoods were next clustered using a SOM, with the number of regions automatically determined by the Davies-Bouldin criterion. This resulted in generation of 10 distinct tissue regions (color bar at the top of Fig. 3d) that were enriched with different cell types, suggesting a relatively discrete distribution of cells within the LNs. Positional remapping of the neighborhoods, color-coded by region, directly recapitulated the spatial boundaries and the general architectural features seen qualitatively in the original image, suggesting robust digital tissue reconstruction (Fig. 3e, S3a, S3b). This analysis also demonstrated that the different DC and macrophages subsets appeared relatively segregated from one another within distinct spatial compartments, corroborating previous observations.[4] Region visualization also established the predominant localization of the SIRPa$^-$ migratory dDC population (R4 region) in the lower cortical ridge bordering the LN medulla (Fig. 3e, S3a, S2b).

To further delineate the distribution of different cell types across physiologically defined LN compartments, we used CytoMAP to manually annotate the tissue regions based on landmark spot clustering (Fig. 3d, S2b, S3c). This resulted in new composite regions, color annotated at the bottom of the heatmap in Fig. 3d, with region R1 corresponding to B cell follicles, region R2 to the sub-capsular sinus (SCS), regions R3-R7 to the T cell zone and Interfollicular zones (TZ+IFZ), region R8 to the sinus, and regions R9 and R10 to the cortico-medullary cords (CMC) (Fig. 3d, 3e, S3c). Next, using the *Make Surface* function in CytoMAP, we built surfaces around the neighborhoods belonging to these annotated groups (Fig. 3f), then calculated the distances of the myeloid cell populations to the borders of these surfaces (Fig. 3g, S3e). The distance to each region border for all cells in a single sample (Fig. 3g, S3e) or averaged over all cells for multiple samples (Fig. 3h-3j, S3f), corroborated the qualitative observation that most DCs were distributed within the TZ+IFZ, while the macrophages were positioned in either the SCS or CMC. This analysis also confirmed preferential localization of resident cDC2s in closer proximity to the CMC and B cell follicles, compared to the more heterogeneous distribution of resident cDC1s within the LN (Fig. 3i, 3j). Additionally, distance analysis revealed that CD301b$^+$ DCs were primarily distributed in close proximity to the B cell follicles, as previously described,[45] while the SIRPa$^-$ migratory dDCs were located distally from the B follicles and in close proximity to the CMC (Fig. 3i, 3j, S3f).

The fairly discrete clustering and spatial segregation of different myeloid cell types in distinct tissue regions (Fig. 3d, 3e) also indicated that the DC subsets were distributed in spatially non-overlapping regions across the TZ+IFZ. To explore the spatial exclusivity of DC populations, the Pearson correlation coefficients of the number of cells per neighborhood, averaged over all of the samples, was calculated in CytoMAP for either all neighborhoods or only the neighborhoods in the TZ+IFZ regions (Fig. 3k, S3g). Whole tissue correlation analysis demonstrated that all DC populations in general were positively correlated with CD3 spots and negatively correlated with Lyve1 spots and medullary macrophages (Macs), indicating that on average, most DCs are positioned in the T cell zone and not in the LN medulla (Fig. 3k left). LN resident cDC2 and SCS Macs were also positively correlated with B220 spots, in line with their enhanced prevalence in the interfollicular regions and lining the B cell follicles, respectively. Correlation analysis of the TZ+IFZ compartment, enriched in most DC populations, further revealed that migratory DC populations (i.e. CD207^{+} DCs, CD301b^{+} dDCs, SIRPa$^{+/-}$ dDCs) were either negatively correlated with one another or displayed little spatial correlation, thus quantitatively supporting the observation of spatial segregation of these DC subsets in LNs seen by clustering (Fig. 3d, 3k right). Together, these analyses highlight the ability of CytoMAP to delineate complex patterns of cellular organization into quantitative metrics. Biologically, these observations reveal strong spatial exclusivity for different DC populations, as well as identify the distribution profile of migratory SIRPa^{-} dDCs.

Spatially organized myeloid cell associations with LN blood vessels

In addition to the myeloid cell segregation, qualitative examination of imaged LN sections revealed that some DC populations appeared to be spatially associated with LN blood vessels in specific tissue compartments. Given the established role of DCs in homeostatic maintenance of LN vasculature for proper immune recirculation, we examined the relative distribution of DC subsets with respect to LN blood vessels.[27,28] To account for the sampling error associated with thin section imaging, in which critical tissue landmarks may lie just above or below the sectioning plane, we turned to volumetric microscopy of stained and Ce3D optically-cleared 500 μm thick slices of steady state murine LNs.[13,35] This resulted in robust visualization of complex patterns of DC subsets in 3D tissue space (Fig. 4a). Qualitative examination of the imaged LNs revealed close association of the Clec9a^{+} resident cDC1s with CD31^{+} vascular endothelial cells, and many of these DCs appeared to encapsulate large segments of the neighboring blood vessels (Fig. 4a and Video S1). In contrast, CD207^{+} migratory DCs (Langerhans cells and migratory cDC1s) appeared less associated with the LN vasculature. To quantitate these observations, we performed histo-cytometry to identify various DC and macrophage populations and passed the positional data of these cells to CytoMAP (Fig. S4a, S4b).[13,35] As above, positional information on the B220^{+} B cell follicles and Lyve1^{+} lymphatic sinus landmark spots were also imported for analysis. To provide positional information on CD31^{+} blood vessels, we generated segmented surface objects on the CD31 channel and imported these objects' data into CytoMAP. Additionally, RDPs were defined throughout the 3D LNs for comparison to the myeloid cell distribution. The distances for the different myeloid cell subsets or RDPs to the nearest blood vessel object were next calculated using CytoMAP (Fig.

4b). Visualization of the individual cell distances to the closest blood vessel demonstrated that, while there was substantial heterogeneity within a given cell population, both resident cDC1 and cDC2 populations were on average located in close proximity to blood vessels (Fig. 4a-d). This was in contrast to more distal relationships for most migratory $CD207^+$ DCs, macrophages (Macs), or RDPs. To further explore the relationships between DCs and blood vasculature, we calculated the Pearson correlation coefficients for the number of cells per 50μm radius neighborhood. This analysis demonstrated that in contrast to migratory DCs, resident cDC1 and cDC2 subsets were both positively correlated with blood vessels (Fig. 4e, S4c). These data indicate that resident DCs are spatially associated with LN vasculature, which supports the hypothesis that blood vessels may provide guidance cues to determining the localization of these populations in LNs.

The spatial segregation of resident cDC1 and cDC2 subsets into distinct regions of the LN (Fig. 3c, S3b) also suggested that blood vessels may be differentially associated with specific DC populations across the distinct tissue compartments. To explore the cellular microenvironments associated with the complex vascular networks in LNs (Fig. 5a), we utilized the *Cell Centered Neighborhoods* function in CytoMAP, which instead of raster scanning neighborhoods, generates neighborhoods centered on the positions of the selected objects. This analysis approach provides a more focused interrogation of the cellular relationships for the selected population of interest. Here, 20 μm radius spherical neighborhoods were centered on the $CD31^+$ vascular objects to selectively identify vascular-associated myeloid cell populations (Fig. 5b). This *Cell Centered* approach is demonstrated in Fig. 5b, in which white dots demarcate the centers of all blood vessel objects within the zoom image, and with the example 2D projections of the spherical neighborhoods shown to surround several distinct vascular objects (yellow dots). Once generated, these neighborhoods were clustered using the SOM algorithm, with the number of regions determined automatically using the Davies-Bouldin criterion (Fig. S5a). This clustering separated the vascular neighborhoods into several distinct region types (Fig. 5c, top color bar, S5b). These were next manually grouped into four major blood vessel phenotypes based on the local DC subset composition (Fig. 5c, bottom color bar). This analysis revealed that, while many neighborhoods were not closely associated with any given myeloid cell type (unassociated), large portions of the vascular neighborhoods were preferentially associated with either the resident cDC1 or the cDC2 subset. A small number of neighborhoods were also associated with $CD207^+$ migratory cells (Fig. 5c, S5c). Importantly, 3D spatial remapping of the different vascular subtypes in CytoMAP revealed that large segments of the vascular branches were associated with either the resident cDC1 or cDC2 subset, with little local spatial intermixing (Fig. 5d, Video S2). These data suggest that the spatial segregation of DC subsets and their association with local blood vessels encompass discrete segments of the LN vascular branches that are preferentially associated with one or another DC population, indicating potential mechanisms for vascular heterogeneity.[29,30]

CytoMAP analysis of the tumor microenvironment

Thus far, CytoMAP was used to explore cellular spatial relationships in tissues with relatively well-established structural organization. However, one area where advanced image analysis may

provide substantial benefit is in cancer research, in which isolated tumor biopsies have poorly understood cellular organization but still possess substantial prognostic value. We thus tested the capabilities of CytoMAP in exploring the distribution of immune cells in tumors from a murine syngeneic CT26 colorectal cancer model. For these studies, isolated CT26 tumor sections harvested from a Balb/C mouse 16 days after implantation were stained with a panel of markers to detect various innate and adaptive immune populations and imaged (Fig. 6a). Histo-cytometry was used to gate on T effector cells (Teff), T regulatory cells (Treg), B cells, tumor associated macrophages (TAMs), activated macrophages (aMacs), DCs, and MHC-II^{+} SIRPa^{DIM} myeloid cells (Fig. S6a). The positional data for these cells were next imported into CytoMAP for further analysis. Spatial replotting of the cell populations revealed striking compartmentalization of the tumor tissue into areas enriched with different immune cell subsets (Fig. 6b). SOM clustering of 50μm raster scanned neighborhoods identified tissue regions preferentially associated with specific myeloid cell populations (Fig. 6c, S6b). This was visualized by spatial remapping of the clustered regions, revealing discrete tumor zones composed of spatially segregated region types and the associated cell subsets (Fig. 6d). As an example, region R6 was predominantly composed of DCs and Teff cells, and was primarily localized to the outer periphery of the tumor (Fig. 6c, 6d), resembling the lymphocytic cuff previously observed in colorectal and other cancers.[32] In contrast, regions R2 and R3 were dominantly composed of TAMs, and these regions were localized within the deeper portions of the tumor tissue (Fig. 6c, 6d). To better understand the spatial relationships among these tumor microenvironments, we next utilized the *Pseudo-space* function in CytoMAP. For this, smoothed distributions of neighborhoods enriched in DCs were sorted to the left and those enriched in TAMs were sorted to the right along the Pseudo-space axis. This analysis helped visualize the underlying distribution of the different immune subsets within these tumors, demonstrating increased abundance of TAMs in the neighborhoods more proximal to the tumor core, and with increased presence of lymphocytes and DCs in the tumor periphery, thus representing the immune cuff (Fig. 6e). Interestingly, Teff cells were well-represented in both the peripheral immune cuff and the tumor core, while the Tregs were predominantly restricted to the outer tumor periphery. This indicates that this CT26 sample represents a relatively well-infiltrated 'hot' tumor that may be susceptible to checkpoint blockade therapy, which is consistent with published observations.[47,48] These spatial relationships were further quantified using the Pearson correlation coefficients of the number of cells per neighborhood (Fig. 6f, S6c). This demonstrated positive correlation of T and B cells with DCs and aMacs, and negative correlation with TAMs, thus revealing the local cellular networks and the preferential associations of different cell types across the distinct tumor microenvironments. Notably, the negative correlation of Teff cells and TAMs indicated that while the Teff cells were generally capable of infiltrating the tumor tissue, they were not enriched in the areas dominantly populated with TAMs, which can also be seen in the Pseudo-Space plot, in which the Teff numbers drop in the TAM-associated neighborhoods (Fig. 6e). Collectively, these data reveal marked segregation of different myeloid cell types across the tumor tissue, as well as demonstrate that the different analytical modules in CytoMAP can be successfully used to study cellular localization within complex tissues.

CytoMAP reveals underlying organization of immune cells in Mtb granulomas

In addition to tumors, previous studies have demonstrated structured organization of immune cells within Mtb-infected pulmonary granulomas.[33,49–52] We thus tested the ability of CytoMAP to quantitatively explore such organization in a 20μm lung section from a mouse infected with aerosolized Mtb. We observed formation of a discrete Mtb-associated lung granuloma and complex patterns of cellular distribution within this structure (Fig. 7a). Two regions of interest, one of the unaffected lung and one of the Mtb-infected granuloma (Fig. 7a), were imaged at high resolution for in depth analysis. As before, histo-cytometry was used to gate on the different cell populations, including $CD4^+$ and $CD4^-$ T cells, B cells, $CD11b^+$ myeloid cells, alveolar macrophages (Alv. Macs.), DCs, and Mtb^+ infected cells (Fig. S7a). The positions of these cells were next passed into CytoMAP for remapping (Fig. 7b) and analysis. A small number of the Mtb^+ objects were identified outside the granuloma in the images. These appeared extra-cellular and likely represented imaging artifacts; they were not selectively removed from analysis to avoid introducing user bias. Heatmap visualization of the clustered, 50μm radius raster scanned neighborhoods, with automatic region number identification, revealed distinct region types composed of different immune cell populations (Fig. 7c, S7b, S7c). Remapping of the region color-coded neighborhoods demonstrated that the neighborhoods enriched in Mtb-infected myeloid cells (R3) were primarily located in the deep center of the granuloma (Fig. 7d), recapitulating visual observations. These infected regions were surrounded by neighborhoods containing high concentrations of T cells (R4 and R5), and these were further surrounded by regions associated with uninfected myeloid cells and Alv. Macs. (R2). We also detected segregated B cell rich neighborhoods in region R6 (Fig. 7d), which were reminiscent of B follicles and tertiary lymphoid structures. To further examine these cellular relationships, we performed Pseudo-space analysis (Fig. 7e). This plot demonstrated that within the granuloma, T cell and B cell rich neighborhoods were concentrated just outside of the core infected Mtb^+ cells. The Alv. Macs and DC-rich neighborhoods also appeared excluded from the central core of the granuloma, recapitulating the image data. These relationships were also quantitatively explored by calculating the Pearson correlation coefficients of the numbers of cells in the neighborhoods (Fig. 7f, S7d). In this analysis, the left half of the heatmap, representing uninvolved lung tissue, demonstrated no strong correlations between the different immune cell types, consistent with qualitative observations (Fig. 7a, 7b). In contrast, the right half of the heatmap, representing the granuloma, demonstrated positive correlation between the Mtb^+ infected cells and the $CD11b^+$ myeloid cells, weaker correlation with the surrounding T cells, and negative correlation with Alv. Macs. These findings are consistent with previous observations of immune cell organization in Mtb granulomas, describing the partial segregation of $CD4^+$ T cells from Mtb-infected cells and the formation of tertiary lymphoid structures. Collectively, these data indicate that CytoMAP is capable of robust analysis of highly complex tissue structures across diverse organ types and disease settings.

DISCUSSION

The importance of quantitative imaging and spatial analysis has emerged across a diverse spectrum of biological disciplines at different length scales; from the localization of single molecules within individual cells to the organization of cells across whole organs. Various technologies allow spatially resolved high-content detection of diverse probe types, from protein and oligonucleotide imaging to mass spectroscopy enabled lipid visualization. These approaches are providing an unprecedented level of detail into biological processes, and the development of better tools for analyzing increasingly complex and voluminous datasets is critical.[4,10,13,14,22,32,35,39,53–55] Here we developed and described a comprehensive analysis platform, CytoMAP, capable of robust spatial analysis of cellular organization within tissues. CytoMAP harnesses the power of data clustering, dimensionality reduction, and advanced data visualization to expand the utility of spatially resolved cellular profiling. CytoMAP integrates data on cellular phenotypes and positioning to identify unique neighborhoods and structures within tissues and organs, which provides the ability to compare complex spatial patterns across heterogeneous samples. While our technology is demonstrated here using histo-cytometry generated data on cell positioning, CytoMAP in principle can be utilized with datasets generated by diverse imaging-based approaches and for analysis of various target structures at different length scales. Here we utilized CytoMAP to explore and quantify the organization of immune cells and encompassing microenvironments within lymphoid tissues, as well as in tumor and Mtb-infected lung samples. Our results indicate a robust ability of CytoMAP to reveal well-established and previously unappreciated cellular organization within these tissues. In particular, our studies identified the localization of SIRPa^{-} migratory dDCs within the lower cortical ridge of the T cell zone bordering the LN medulla, as well as reveal preferential associations of LN-resident DC populations with blood vessel networks in distinct LN compartments.

In contrast to other approaches, CytoMAP substantially reduces data complexity in two major ways. First, CytoMAP treats complex cell objects as individual points, each possessing information on the positional, morphological and phenotypic cellular characteristics averaged over their respective 3D segmented cellular bodies. Second, CytoMAP defines raster scanned, or cell-centered, local neighborhoods across the tissue, effectively binning data on many similarly positioned cells into a single neighborhood. Biologically, such neighborhood binning is equivalent to the concept that, much like urban environments, tissues are subdivided into local microenvironments or neighborhoods containing specific interacting cell populations. Computationally, both steps dramatically reduce the data size (~ 3 orders of magnitude), allowing rapid comparative analysis of cellular composition within the neighborhoods and investigation of how these tissue building blocks are spatially patterned across large 2D and 3D samples. The ability to manipulate the size of the neighborhoods also provides the user with the ability to rapidly explore overarching tissue structure or to perform detailed investigation of the hyperlocal cellular microenvironments and cell-cell interactions. Using SOM data clustering, similar neighborhoods are grouped together via topological analysis, which computationally defines unique tissue regions within highly complex datasets with minimal user input. Once clustered, CytoMAP provides tools for exploring the cellular composition and relative prevalence of the tissue regions within and across samples, as well as for visualizing these regions in 2D or 3D space. Interaction network maps provide additional detail into how the regions are spatially interconnected with one another to generate global tissue structure.

Additional tools provided in CytoMAP allow the user to utilize dimensionality reduction algorithms on tissue neighborhoods to examine the heterogeneity of individual or multiple samples, as well as to assess the general principles of neighborhood spatial organization. Finally, neighborhood based correlation analysis facilitates exploration of how different cell populations are spatially correlated with one another, revealing local cellular interactions, or mutual exclusivity of different cell types with one another. In addition to whole tissue analysis, CytoMAP allows examination of cell-cell correlations within specified tissue regions, which may be important if cells have different interaction properties in distinct tissue compartments. Together, the combination of comprehensive and flexible analytical approaches built into a user-friendly interface makes CytoMAP a powerful tool for exploration of complex cellular spatial relationships within large multiplexed imaging datasets.

Analysis of the organization of myeloid cells in steady state murine LNs with CytoMAP generated a quantitative depiction of the distribution profiles of distinct innate immune subsets. Consistent with previous observations, we found extensive spatial segregation and a high degree of mutual exclusivity for many of the DC subsets within distinct sub-compartments of the LN. In addition, we identified the spatial distribution of a recently described SIRPa^{-} migratory dDC population, which, to our knowledge, has not been positionally mapped.[25,26] We found that these migratory dDCs are predominantly localized within the lower cortical ridge bordering the LN medulla, and together with the locally positioned SIRPa^{+} dDCs generate a prominent cuff-like cellular aggregate. Furthermore, quantitative analysis of resident cDC1 and cDC2 organization recapitulated previous findings, with preferential localization of resident cDC2 in the LN periphery and with more heterogeneous distribution of resident cDC1s across different LN compartments, including the T cell zone and some presence in the LN medulla.[4,5,7–9,44,56] Intriguingly, as revealed by 3D vascular based neighborhood analysis, we found that both resident cDC1 and cDC2 subsets were also highly associated with LN blood vessels. Given the spatial segregation of these DC populations to different LN regions, we found that resident cDC1s and cDC2s were also associated with distinct vascular trees, with little local intermixing. While previous studies have shown that during inflammation, DCs can associate with blood vessels,[57,58] here we demonstrate that this blood vessel association also occurs in steady state tissues, and this may be involved in promoting homeostatic maintenance of LN blood endothelial cells.[27,28] Additionally, our studies suggest that distinct localized cellular interactions may bidirectionally shape both DC and blood endothelial cell biology, potentially promoting the extensive heterogeneity of LN blood endothelial cells, as recently described in a dissociation-based single-cell mRNA study.[29] This differential DC subset localization with blood vessels has the potential to also influence heterogeneity in cellular recruitment. Understanding the molecular regulation of such complex cellular patterning and interactions of different innate and stromal cells requires further study, but likely involves an interplay of multiple different chemotactic and adhesive cues within the LN. While previous studies have identified a role for the G-protein coupled receptor 183 in guiding resident cDC2 positioning and survival in lymphoid tissues,[59,60] little is known about the regulation of resident cDC1 localization during homeostasis. Our studies indicate that blood vessels could provide such positional cues to guide resident cDC1 distribution in steady state LNs.

In addition to lymphoid tissue organization, we used CytoMAP to explore the organization of immune cells in a CT26 tumor sample. This analysis identified several hallmark features of tumor architecture, including a lymphocytic cuff, as well as centralized positioning of

TAMs, which corroborates previous histological studies.[32] CytoMAP also revealed moderate-to-high baseline infiltration of CT26 tumors by effector T cells, suggesting that this cancer model should be susceptible to checkpoint blockade therapy, which is in line with published data.[47,48] Interestingly, we found that different myeloid cell types lie in distinct regions within the tumor, suggesting additional layers of cellular organization that should be explored in future mechanistic studies. Visualizing these relationships across whole tumor cross-sections also revealed substantial intratumoral heterogeneity with respect to the local composition of myeloid cells and lymphocytes. This suggests that accurate risk/prognostic assessment of neoplastic tissues may benefit from access to larger tissue samples in addition to the limited-in-size punch core biopsies.

As a final test of CytoMAP, we analyzed cellular organization within granuloma structures in a murine Mtb-infected lung sample. We observed partial segregation of infiltrating $CD4^+$ T cells from Mtb-infected myeloid cells, and formation of B cell aggregates. Presence of these distinct tissue regions as identified by CytoMAP's clustering algorithm largely agrees with previous studies describing immune cell organization in Mtb granulomas, suggesting that CytoMAP presents a promising avenue for investigating the spatial organization of cells in inflamed and infected tissues.[34]

In sum, here we develop a user-friendly, comprehensive, and broadly applicable spatial analysis toolbox for analysis of 2D or 3D quantitative imaging datasets, which excels at utilizing high-dimensional imaging data to reveal complex tissue features based on cellular phenotypic heterogeneity and spatial patterning. Our technology allows robust cross-sample interrogation of cellular spatial relationships, tissue architecture, and reveals intra- as well as inter-sample heterogeneity. In this early implementation, CytoMAP has already provided new insights into the organization of myeloid cells in lymphoid tissues, revealing the localization of $SIRPa^-$ migratory dDC, as well as identifying preferential associations of resident DCs with select LN vasculature. Together, this indicates that CytoMAP is a valuable tool for the rapid identification of key cellular networks and tissue structure, revealing the fundamental building blocks of tissue organization.

ACKNOWLEDGMENTS

We thank Dr. Frank Schmitz (Celgene/Fred Hutch) for many useful discussions. We additionally thank the open source software community, including HistoCat, Flow Cytometry GUI for Matlab, fca_readfcs (fca 2.2). This work was in part funded by Roche Glycart, the Washington Research Foundation postdoctoral fellowship (CS), and NIH grants R01AI134713 (MYG), R21AI142667 (MYG), 1R01AI134246 (KBU), 1R01AI076327 (KBU), U19AI135976 (KBU), T32HD007233 (BHG).

AUTHOR CONTRIBUTIONS

CS and MG analyzed data and prepared manuscript. CS and JF wrote the software. CS and MG conceived of the project and software. CS, BO, JL, BG, MG, and CP performed mouse studies and imaged samples BO and MG Validated Antibodies. MP and TP provided tumor samples. BG, CP, and KU provided lung samples. CS, JF, BO, BG, MLC, BEO, JL, CPS, TP, MP, JH, and MG provided software feature, design, and usability feedback. CS, CPS, MG, and JF

conceived of and implemented statistical approaches. MG supervised the project. All authors edited manuscript.

COMPETING FINANCIAL INTEREST

MP and TP are employees of Roche. CS, JF, MLC, BO, JL, JH, BG, CPS, KU, CP and MG declare no financial interests.

DATA AVAILABILITY

CytoMAP software is available for download at https://gitlab.com/gernerlab/cytomap. Imaris extensions and other code used for histo-cytometry analysis is available for download at: https://gitlab.com/gernerlab/imarisxt_histocytometry. All data are available upon request.

Methods

LEAD CONTACT AND MATERIALS AVAILABILITY

Further information and requests for resources and reagents should be directed to and will be fulfilled by the Lead Contact, Michael Y Gerner (gernermy@uw.edu).

EXPERIMENTAL MODEL AND SUBJECT DETAILS

Mice

For the experiments described in Fig. 2-5, 6-10 week old male and female B6.SJL and C57BL/6J mice were obtained from The Jackson Laboratory and kept in specific pathogen–free conditions at an Association for Assessment and Accreditation of Laboratory Animal Care–accredited animal facility at the University of Washington, South Lake Union campus. All procedures were approved by the University of Washington Institutional Animal Care and Use Committee.

For the experiment described in Fig. 7, C57BL/6J mice were obtained from The Jackson Laboratory and housed in specific pathogen-free conditions at Seattle Children's Research Institute (SCRI). Experiments were performed in compliance with the SCRI Animal Care and Use Committee. An 8 week old female mouse was used for the presented study.

METHOD DETAILS

LN studies

For the experiment shown in Fig. 2, a C57BL/6 mouse was adoptively transferred with 10^6 naïve OT-II CD4+ T cells and one day later immunized in the footpad with OVA plus Alum; 4.5 days later the draining popliteal LN was harvested and used for analysis. For the experiments shown in Fig. 3, non-draining steady state skin LNs were harvested from C57BL/6 mice which were previously injected in the contralateral distal footpad with Alum 2 days before harvest. For the experiments shown in Fig. 4 and 5, skin LNs were harvested from naïve C57BL/6 mice.

Tumor studies

Balb/C mice were injected with CT26 cells and 16 days later, the tumor was harvested for fixation and imaging.

Mtb studies

All infections were done with a stock of Mtb H37Rv, as previously described.[61] To perform aerosol infections, C57BL/6 mice were enclosed in a Glas-Col aerosol infection chamber, and Mtb bacilli were deposited directly into their lungs. Lungs were removed at the specified timepoint.

Tissue preparation – thin sections

All thin tissue sections were fixed with Cytofix (BD Biosciences) buffer diluted 1:3 with PBS for 12h at 4° C and then dehydrated with 30% sucrose in PBS for 12-24h at 4° C. Tissues were next embedded in O.C.T. compound (Tissue-Tek) and stored at -80° C. LNs were sectioned on a Thermo Scientific Microm HM550 cryostat into 20µm sections and were then prepared and imaged as previously described.[4] Briefly, sections were stained with panels of fluorescently conjugated antibodies, shown in Table 5, cover-slipped with Fluoromount G mounting media (SouthernBiotech), and imaged on a Leica SP8 microscope.

Tissue preparation – thick slices

For volumetric imaging using Ce3D tissue clearing (thick tissue sections), experiments were performed as previously described.[13,35] In brief, LNs were fixed with Cytofix (BD Biosciences) buffer diluted 1:3 with PBS for 12-20h at 4° C. Excess fat was carefully removed using a dissection microscope, and the samples were embedded in Agarose (0.2g agarose + 10ml DI water). 500um thick cross-sectional slices were generated using a Vibratome (Leica VT1000S, Speed: 215 Frequency: 8). Slices were next placed in blocking buffer (1%NMS, 1%BSA, 0.3%Triton, in 0.1MTris) for 24 hours at room temperature on a rocker. After blocking, LN slices were stained with a panel of directly conjugated antibodies (table 5) for 3 days at 34C on a shaker, then washed in blocking buffer for one day at 24C. Next, slices were placed in Ce3D clearing solution (13.75ml 40% [vol/vol diluted with PBS] N-methylacetylamide; 20g Histodenz; 25uL Triton X-100; 125ul Thioglycerol) at room temperature for at least 24 hr. Finally, slices were cover-slipped using Ce3D as the mounting media and imaged on a Leica SP8 microscope.

Imaging

All samples were imaged using a Leica confocal SP8 microscope, with either a 40X 1.3NA (HC PL APO 40x/1.3 Oil CS2, for 20µm sections) or a 20X 0.75NA (HC PL APO 20x/0.75 IMM CORR CS2, free working distance = 0.68 mm, for thick cleared slices) oil objective with type F immersion liquid (Leica, refractive index n_e = 1.5180). After acquisition, images were stitched together and compensated for spectral overlap between channels using the Leica Channel Dye Separation module in the Leica LASX software. For acquisition of single stained controls, UltraComp beads (Affymetrix) were incubated with fluorescently conjugated antibodies, mounted on slides, and imaged with the same microscope settings used in the image they were being used to compensate.

QUANTIFICATION AND STATISTICAL ANALYSIS

Image analysis and histo-cytometry

Histo-cytometry was performed as described previously, with minor modifications.[4,13,35] Briefly, using Imaris, various steps were taken to process the images and segment the cell objects. Unless otherwise noted, only the channel arithmetic and surface creation steps for each sample shown in Tables 2 and 3 were used to process the images. Channel arithmetic were performed using either the default Imaris function or a customized ImarisXT extension, *Calebs_Multi_EQ_ChannelArithmetics_V3* (available online), which allows for batching multiple equations and auto saving the image once the function is done

running. Additional normalization and processing steps for specific samples are described below. After surface creation, the MFI for each imaged channel, as well as the volume, sphericity, and position of the cell objects were exported and concatenated into a single .csv file using the *Imaris_To_FlowJo_CSV_Converter_V4* MATLAB function, which is a customized .csv merge tool available online. The combined .csv file was next imported into FlowJo (TreeStar) and the cell objects were classified into the indicated cell subsets according to the gating strategies shown in the respective figures.

For the experiments described in Fig. 2, using Imaris version 8.3 the All Cell Composite channel was created using the equation in table 2. Using the surface creation tool in Imaris, masking surfaces were created around this new channel using the parameters for surface_1 shown in table 3. Using the mask option, all pixels from the new channel outside the boundaries of this surface were set to equal 255 (the maximum pixel intensity). Next the new channel was smoothed with a Gaussian filter with a width of 0.56μm. This new channel was then inverted, and the gamma was set to 0.3. Finally, cell object surfaces were created using the inverted new channel with the properties shown in table 3 for surface_2.

For both experiments shown in Fig. 4, all image layers were first normalized along the Z axis. For experiment 1, a clean CD31 channel was created to correct for residual channel spillover from the Lyve1 channel. Next a composite channel of myeloid cell markers was created according to the equation in table 2. Finally, surfaces were created according to the parameters in table 3. For the images from the second experiment, channels SIRPa, B220, MHC-II, CD31, and CD11c were smoothed using the Imaris *Gaussian Smooth* function with a width of 0.56μm. Next, a composite channel of myeloid cell markers was created according to the equation in table 2. Finally, surfaces were created according to the parameters in table 3.

For the image of the lung shown in Fig. 7, a composite of all surface markers was created using the equation in table 2. The linear stretch function in Imaris was used to set the blackpoint of this channel to 40, gamma was adjusted to 0.75, and Gaussian smoothing was used with a width of 0.32um. The Jojo1 nuclear stain channel was brightened with the linear stretch function in Imaris to set the saturation point to 200, gamma was adjusted to 1.5, and Gaussian smoothing was used with a width of 0.32um. The all surface marker channel was then subtracted from the altered Jojo1 channel to form a “Nuclei” channel according to table 2. Finally, surface objects were created in Imaris on this new channel using the parameters outlined in table 3.

Statistical analysis

No statistical method was used to predetermine sample size. The statistical significance of Pearson's correlation was calculated using a Student's t distribution for a transformation of the correlation.

CytoMAP spatial analysis

CytoMAP was written using MATLAB version 2018b (Mathworks). A detailed description of the workflow and functions built into CytoMAP is available in the online user manual. Briefly, the analysis used for the datasets described in this manuscript went as follows. The annotated cell surfaces for each dataset were loaded into CytoMAP by importing the corresponding paired .wsp and .fcs files after saving them in FlowJo. These collectively contain the cell statistics, gate definitions, and spatial positions for each cell object. Once imported the following functions were used in CytoMAP to analyze the data.

Generate Random Points

This function, found in the ribbon at the top of the figure window, uses MATLAB’s built in *rand* function, with all default parameters, to generate a set of random points based on the set of currently

plotted points in the *New Figure* window. This function only generates randomized data with respect to the axes which are plotted, while setting all other channel values to 0 for the new set of points. Additionally, this function scales the randomized values to be within the limits of the currently plotted points. To generate points with a random spatial distribution, all cells were first plotted with positions on the X and Y axes. Next, the Generate Random Points function was called and this newly generated set of points was saved. Finally, all points outside the spatial bounds of the tissue were discarded by gating on objects within the tissue boundaries, resulting in sets of RDPs for each sample analyzed, with a representative set of points shown in Fig. S2b.

Make Surface

This function uses MATLAB's *alphaShape* function, with user defined parameters, to wrap the currently plotted points in a surface. This surface can then be used to gate on points, such as randomly distributed points, and to calculate the distance to region borders. This function was used to generate the surfaces shown in Fig. 3f.

Calculate Distance

This function finds the physical distance, either to the border of user defined surfaces, or to the nearest cell. This function was used to find the distance to region borders plotted in Fig. 3 g-j, and the distance between myeloid cells and the nearest blood vessel plotted in Fig. 4b.

Raster Scan Neighborhoods

This function uses Neighborhood analysis, which finds the local composition of cells within a circular (2D data) or spherical (3D data) area/volume in the tissue. If the data has non-zero z dimensionality but the z thickness is less than the radius of the neighborhoods, this function will treat the data as effectively 2D and use a cylindrical neighborhood window. This function calculates the number of cells and the MFI of each channel summed over all cells in each neighborhood. The positions of the neighborhoods are evenly distributed throughout the tissue in a grid pattern with a distance between neighborhood centers of half of the user defined radius. The neighborhood information can then be used for further analysis (e.g. local cellular densities, cell-cell associations).

Cell Centered Neighborhoods

This function is similar to *Raster Scan Neighborhoods*, except the position of the neighborhoods are centered on a user selected cell type. Once the cell type is chosen and the radius is defined, this function calculates the number of cells and the MFI of each channel summed over all cells in each neighborhood.

Classify Neighborhoods Into Regions

This function is used to define tissue regions using multiple types of information about the neighborhoods. This includes, the standardized number of cells of each phenotype in each neighborhood (number of cells minus mean number of cells, divided by the standard deviation of the number of cells in each neighborhood across the dataset), composition (number of cells divided by the total number of cells in each neighborhood) and raw number of cells per neighborhood, which were used as indicated in the respective figures. In this manuscript, the physical position of the neighborhoods was not used for region definition and the minimum of the Davies-Bouldin function was used to automatically determine the number of regions. The neighborhoods were clustered using the SOM function. This function utilizes MATLAB's *selforgmap* internal function with default parameters, except the dimensions options, which is equal to the number of regions (NR) by one, i.e.

app.net.(ModelName).Network = *selforgmap([NR, 1])*

Once the network parameters are defined, the network is trained on the neighborhood data using MATLAB's *train* function. This assigns a cluster number to each neighborhood. The *selforgmap* algorithm starts with NR "neurons" positioned throughout the data. It then iteratively moves the position of the neurons closer to the data to match the landscape of the data. Here, the position is not the spatial position, but the topological position within the cell composition data. The neighborhoods are then clustered by finding the closest neuron for each neighborhood. For visualization purposes the arbitrarily color designations of the individual regions were changed using the *Edit Region Colors* function in CytoMAP. The composition of the color-coded neighborhoods was plotted using the *Heatmap Visualization* function in CytoMAP. The spatial distribution of the regions was visualized by generating a new figure in CytoMAP, plotting the positions of the neighborhoods, and selecting the regions for the 'c' axis to color-code the neighborhoods by region type.

Reduce Dimensions

This function uses the built in MATLAB implementation of the t-SNE algorithm to reduce the neighborhood data to two dimensions. For the t-SNE plots in this manuscript the default MATLAB options were used, including: Euclidian distance, perplexity of 30, theta, of 0.5, and exaggeration of 4.

Pseudo-Space

This function allows the user to sort the neighborhoods by the absolute number or composition of different cell types within the neighborhoods and plots the neighborhoods in this sorted order on a linear pseudo-space axis. The Y axis is normalized to allow comparison between cell types, and the data are smoothed along the X axis by a user defined amount. This function was used with the data type, weights, and smoothing parameters for each figure shown in Table 4.

Cell-Cell correlation analysis

This function calculates the Pearson correlation coefficient of the number of cell or object types within the scanned neighborhoods and graphs these on a heatmap plot.

Network Map

This function calculates the percentage of neighborhoods of each region type which are directly in contact with each other region type. It creates a force directed graph with a node for each region type, where the nodes are connected by an edge if more than 0.005% of the neighborhoods of that nodes type are in contact with the connecting node's region type. The edge thickness is proportional to the % of neighborhoods in contact with the connecting node region type, and the node size is proportional to the number of neighborhoods of the region type.

DATA AND CODE AVAILABILITY

Imaris extensions and other scripts used for histo-cytometry analysis are available for download at: https://gitlab.com/gernerlab/imarisxt_histocytometry

CytoMAP software is available for download at:
https://gitlab.com/gernerlab/cytomap

All data are available upon request.

REFERENCES

1. Groom, J. R. Regulators of T cell fate: Integration of cell migration, differentiation and function. *Immunol. Rev.* **289**, 101–114 (2019).
2. Qi, H., Kastenmüller, W. & Germain, R. N. Spatiotemporal Basis of Innate and Adaptive Immunity in Secondary Lymphoid Tissue. *Annu. Rev. Cell Dev. Biol.* **30**, 141–167 (2014).
3. Eisenbarth, S. C. Dendritic cell subsets in T cell programming: location dictates function. *Nat. Rev. Immunol.* **19**, 89–103 (2019).
4. Gerner, M. Y., Kastenmuller, W., Ifrim, I., Kabat, J. & Germain, R. N. Histo-Cytometry: A Method for Highly Multiplex Quantitative Tissue Imaging Analysis Applied to Dendritic Cell Subset Microanatomy in Lymph Nodes. *Immunity* **37**, 364–376 (2012).
5. Gerner, M. Y., Torabi-Parizi, P. & Germain, R. N. Strategically Localized Dendritic Cells Promote Rapid T Cell Responses to Lymph-Borne Particulate Antigens. *Immunity* **42**, 172–185 (2015).
6. Kissenpfennig, A. *et al.* Dynamics and Function of Langerhans Cells In Vivo: Dermal Dendritic Cells Colonize Lymph Node Areas Distinct from Slower Migrating Langerhans Cells. *Immunity* **22**, 643–654 (2005).
7. Kitano, M. *et al.* Imaging of the cross-presenting dendritic cell subsets in the skin-draining lymph node. *Proc. Natl. Acad. Sci.* **113**, 1044–1049 (2016).
8. Gerner, M. Y., Casey, K. A., Kastenmuller, W. & Germain, R. N. Dendritic cell and antigen dispersal landscapes regulate T cell immunity. *J. Exp. Med.* **214**, 3105–3122 (2017).
9. Baptista, A. P. *et al.* The Chemoattractant Receptor Ebi2 Drives Intranodal Naive CD4+ T Cell Peripheralization to Promote Effective Adaptive Immunity. *Immunity* **50**, 1188–1201 (2019).
10. Goltsev, Y. *et al.* Deep Profiling of Mouse Splenic Architecture with CODEX Multiplexed Imaging. *Cell* **174**, 968–981 (2018).
11. Coutu, D. L., Kokkaliaris, K. D., Kunz, L. & Schroeder, T. Multicolor quantitative confocal imaging cytometry. *Nat. Methods* **15**, 39–46 (2017).
12. Winfree, S. *et al.* Quantitative Three-Dimensional Tissue Cytometry to Study Kidney Tissue and Resident Immune Cells. *J. Am. Soc. Nephrol.* **28**, 2108–2118 (2017).
13. Li, W., Germain, R. N. & Gerner, M. Y. High-dimensional cell-level analysis of tissues with Ce3D multiplex volume imaging. *Nat. Protoc.* **14**, 1708–1733 (2019).
14. Glaser, A. K. *et al.* Multi-immersion open-top light-sheet microscope for high-throughput imaging of cleared tissues. *Nat. Commun.* **10**, 2781 (2019).
15. Schürch, C. M. *et al.* Coordinated cellular neighborhoods orchestrate antitumoral immunity at the colorectal cancer invasive front. *bioRxiv* (2019). doi:10.1101/743989
16. Eng, C.-H. L. *et al.* Transcriptome-scale super-resolved imaging in tissues by RNA seqFISH+. *Nature* **568**, 235–239 (2019).
17. Saka, S. K. *et al.* Immuno-SABER enables highly multiplexed and amplified protein imaging in tissues. *Nat. Biotechnol.* **37**, 1080–1090 (2019).
18. Eliceiri, K. W. *et al.* Biological imaging software tools. *Nat. Methods* **9**, 697–710 (2012).
19. Caicedo, J. C. *et al.* Data-analysis strategies for image-based cell profiling. *Nat. Methods* **14**, 849–863 (2017).
20. Vu, Q. D. *et al.* Methods for Segmentation and Classification of Digital Microscopy Tissue Images. *Front. Bioeng. Biotechnol.* **7**, (2019).
21. Meijering, E. Cell Segmentation: 50 Years Down the Road [Life Sciences]. *IEEE Signal Process. Mag.* **29**, 140–145 (2012).

22. Schapiro, D. *et al.* histoCAT: analysis of cell phenotypes and interactions in multiplex image cytometry data. *Nat. Methods* **14**, 873–876 (2017).
23. Kraus, O. Z., Ba, J. L. & Frey, B. J. Classifying and segmenting microscopy images with deep multiple instance learning. *Bioinformatics* **32**, i52–i59 (2016).
24. Mahadevan, A. S. *et al.* cytoNet: Network Analysis of Cell Communities. *bioRxiv* (2017). doi:10.1101/180273
25. Tussiwand, R. *et al.* Klf4 Expression in Conventional Dendritic Cells Is Required for T Helper 2 Cell Responses. *Immunity* **42**, 916–928 (2015).
26. Ochiai, S. *et al.* CD326 ^{lo} CD103 ^{lo} CD11b ^{lo} Dermal Dendritic Cells Are Activated by Thymic Stromal Lymphopoietin during Contact Sensitization in Mice. *J. Immunol.* **193**, 2504–2511 (2014).
27. Girard, J.-P., Moussion, C. & Förster, R. HEVs, lymphatics and homeostatic immune cell trafficking in lymph nodes. *Nat. Rev. Immunol.* **12**, 762–773 (2012).
28. Moussion, C. & Girard, J.-P. Dendritic cells control lymphocyte entry to lymph nodes through high endothelial venules. *Nature* **479**, 542–546 (2011).
29. Veerman, K., Tardiveau, C., Martins, F., Coudert, J. & Girard, J.-P. Single-Cell Analysis Reveals Heterogeneity of High Endothelial Venules and Different Regulation of Genes Controlling Lymphocyte Entry to Lymph Nodes. *Cell Rep.* **26**, 3116–3131 (2019).
30. Takeda, A. *et al.* Single-Cell Survey of Human Lymphatics Unveils Marked Endothelial Cell Heterogeneity and Mechanisms of Homing for Neutrophils. *Immunity* **51**, 1–12 (2019).
31. Gern, B. H. *et al.* TGFβ restricts T cell function and bacterial control within the tuberculous granuloma. *bioRxiv* 696534 (2019). doi:doi: https://doi.org/10.1101/696534
32. Keren, L. *et al.* A Structured Tumor-Immune Microenvironment in Triple Negative Breast Cancer Revealed by Multiplexed Ion Beam Imaging. *Cell* **174**, 1373–1387 (2018).
33. Plumlee, C. R. *et al.* A blood-based transcriptional signature in a novel murine tuberculosis model predicts risk of human tuberculosis progression. *J Immunol* **200**, 4 (2018).
34. Cadena, A. M., Fortune, S. M. & Flynn, J. L. Heterogeneity in tuberculosis. *Nat. Rev. Immunol.* **17**, 691–702 (2017).
35. Li, W., Germain, R. N. & Gerner, M. Y. Multiplex, quantitative cellular analysis in large tissue volumes with clearing-enhanced 3D microscopy (C $_e$ 3D). *Proc. Natl. Acad. Sci.* **114**, E7321–E7330 (2017).
36. Jiang, J., Trundle, P. & Ren, J. Medical image analysis with artificial neural networks. *Comput. Med. Imaging Graph.* **34**, 617–631 (2010).
37. Vesanto, J., Himberg, J., Alhoniemi, E. & Parhankangas, J. Self-Organizing Map in Matlab: the SOM Toolbox. (2000).
38. Kohonen, T. The self-organizing map. *Proc. IEEE* **78**, 1464–1480 (1990).
39. Gut, G., Herrmann, M. D. & Pelkmans, L. Multiplexed protein maps link subcellular organization to cellular states. *Science* **361**, eaar7042 (2018).
40. van der Maaten, L. & Hinton, G. Visualizing Data Using t-SNE. *J. Mach. Learn. Res.* 2579–2605 (2008).
41. Oyler-Yaniv, A. *et al.* A Tunable Diffusion-Consumption Mechanism of Cytokine Propagation Enables Plasticity in Cell-to-Cell Communication in the Immune System. *Immunity* **46**, 609–620 (2017).
42. Davies, D. L. & Bouldin, D. W. A Cluster Separation Measure. *IEEE Trans. Pattern Anal. Mach. Intell.* **PAMI-1**, 224–227 (1979).
43. Wong, H. S. & Germain, R. N. Robust control of the adaptive immune system. *Semin. Immunol.* **36**, 17–27 (2018).
44. Brewitz, A. *et al.* CD8 + T Cells Orchestrate pDC-XCR1 + Dendritic Cell Spatial and Functional Cooperativity to Optimize Priming. *Immunity* **46**, 205–219 (2017).

45. Kumamoto, Y. *et al.* CD301b+ Dermal Dendritic Cells Drive T Helper 2 Cell-Mediated Immunity. *Immunity* **39**, 733–743 (2013).
46. Sokol, C. L., Camire, R. B., Jones, M. C. & Luster, A. D. The Chemokine Receptor CCR8 Promotes the Migration of Dendritic Cells into the Lymph Node Parenchyma to Initiate the Allergic Immune Response. *Immunity* **49**, 1–15 (2018).
47. Swart, M., Verbrugge, I. & Beltman, J. B. Combination Approaches with Immune-Checkpoint Blockade in Cancer Therapy. *Front. Oncol.* **6**, (2016).
48. Kim, K. *et al.* Eradication of metastatic mouse cancers resistant to immune checkpoint blockade by suppression of myeloid-derived cells. *Proc. Natl. Acad. Sci.* **111**, 11774–11779 (2014).
49. Kahnert, A. *et al. Mycobacterium tuberculosis* Triggers Formation of Lymphoid Structure in Murine Lungs. *J. Infect. Dis.* **195**, 46–54 (2007).
50. Cooper, A. M. Cell-Mediated Immune Responses in Tuberculosis. *Annu. Rev. Immunol.* **27**, 393–422 (2009).
51. Ramakrishnan, L. Revisiting the role of the granuloma in tuberculosis. *Nat. Rev. Immunol.* **12**, 352–366 (2012).
52. Gern, B. & Urdahl, K. TGFB limits T cell function and control of Mycobacterium tuberculosis in granulomas. (2019).
53. Stoltzfus, C. R. *et al.* Two-photon directed evolution of green fluorescent proteins. *Sci. Rep.* **5**, 11968 (2015).
54. Colomb, W., Osmond, M., Durfee, C., Krebs, M. D. & Sarkar, S. K. Imaging and Analysis of Cellular Locations in Three-Dimensional Tissue Models. *Microsc. Microanal.* **25**, 753–761 (2019).
55. Schulz, D. *et al.* Simultaneous Multiplexed Imaging of mRNA and Proteins with Subcellular Resolution in Breast Cancer Tissue Samples by Mass Cytometry. *Cell Syst.* **6**, 25–36 (2018).
56. Leal, J. M., Olin, B. & Gerner, M. Y. Intranodal dendritic cell relocalization during inflammation impacts T cell immunity. *J. Immunol.* **202**, 4 (2019).
57. Bajénoff, M., Granjeaud, S. & Guerder, S. The Strategy of T Cell Antigen-presenting Cell Encounter in Antigen-draining Lymph Nodes Revealed by Imaging of Initial T Cell Activation. *J. Exp. Med.* **198**, 715–724 (2003).
58. Dasoveanu, D. C., Shipman, W. D., Chia, J. J., Chyou, S. & Lu, T. T. Regulation of Lymph Node Vascular–Stromal Compartment by Dendritic Cells. *Trends Immunol.* **37**, 764–777 (2016).
59. Gatto, D. *et al.* The chemotactic receptor EBI2 regulates the homeostasis, localization and immunological function of splenic dendritic cells. *Nat. Immunol.* **14**, 446–453 (2013).
60. Yi, T. & Cyster, J. G. EBI2-mediated bridging channel positioning supports splenic dendritic cell homeostasis and particulate antigen capture. *eLife* **2**, (2013).
61. Urdahl, K. B., Liggitt, D. & Bevan, M. J. CD8 $^{+}$ T Cells Accumulate in the Lungs of *Mycobacterium tuberculosis* -Infected K $^{b-/-}$ D $^{b-/-}$ Mice, But Provide Minimal Protection. *J. Immunol.* **170**, 1987–1994 (2003).

Figure Titles and legends

Figure 1. Workflow and features of CytoMAP. a, Conceptually, tissues are comprised of microenvironments defined by the local composition of different cell populations. CytoMAP is designed to extract quantitative information on cellular localization and composition within imaged samples, revealing how local cell microenvironments are organized to form global tissue structure, as well as allowing robust comparison of intra- and inter-sample tissue heterogeneity. **b**, The workflow starts with multi-parameter imaging of either thin sections or large 3D tissue volumes. Next, hierarchical gating of cell objects generated with existing pipelines is used to annotate distinct cell subsets, which are passed

into CytoMAP for analysis. CytoMAP segments these spatial datasets into individual neighborhoods and uses clustering algorithms to define similar groups of neighborhoods, or tissue 'regions', which can be quantitatively explored and spatially reconstructed in 2D or 3D space. **c**, CytoMAP contains multiple tools to quantify and visualize the tissue architecture across length scales, ranging from analysis of spatial correlations between different cell types, investigation of distance relationships of cells with architectural landmarks, analysis of neighborhood heterogeneity within individual tissues or across multiple samples, as well as quantitative visualization of tissue architecture.

Figure 2. CytoMAP automatically identifies, quantitates and reconstructs major features of LN tissue structure. a, Multi-parameter confocal microscopy image, and zoom-in, of a LN section from an immunized C57BL/6 mouse demonstrating highly compartmentalized staining for B220 (B cells), CD11c (DCs) and CD3 (T cells). Overview image scale bar = 200µm; zoom-in scale bar = 30µm. **b**, Cell objects within the image were segmented and analyzed using histo-cytometry. Plots demonstrate gating used for identification of the indicated immune cell populations. Here, cells with high CD11c MFI are referred to as DCs, albeit this gate may include additional CD11c-expressing cell types. **c**, Cell data from panel b were passed into CytoMAP and positionally plotted (shown area matches panel a zoom-in). CytoMAP was used to raster scan the cells into 30µm radius neighborhoods based on their spatial position, as denoted by the arrow. **d**, Heatmap of the neighborhood cellular composition (percentage of each cell phenotype per neighborhood) after SOM clustering. Individual clusters, 'regions', are denoted by the color bar at the top of the graph. Arrowheads at the bottom highlight the specific neighborhoods also shown in panel c. **e**, Region color-coded positional plot of the neighborhoods from panel d demonstrating general reconstruction of LN architecture. **f**, Pseudo-space plot with the neighborhoods sorted based on B cell composition (sorted to the left) and T cell composition (sorted to the right) on the Pseudo-space axis. This plot demonstrates an abstracted representation of cellular distribution across different LN compartments. **g**, t-SNE plot of the neighborhoods, in which the numbers of cells and total MFI of all channels, but not positional information, were used for the dimensionality reduction. Neighborhoods were color-coded based on region type, as identified in panel d. **h**, Same t-SNE plot as in panel g, but with the neighborhoods color-coded as a heatmap reflecting the number of the indicated cell types per neighborhood. **i**, The t-SNE plot was manually gated based on the cell composition visualized in panel h. **j**, Gated neighborhoods were positionally remapped using the color code definitions from panel i. For this experiment, an imaging volume of 0.03 mm^3, 139,399 cells, and 11328 neighborhoods were analyzed.

Figure 3. CytoMAP reveals diverse patterns of myeloid cell organization in LNs. a, Multi-parameter confocal microscopy image of a representative steady state non-draining LN section from an immunized C57BL/6 mouse. Images demonstrate staining for the indicated myeloid cell markers, with the image on the left also showing B220 (B cells), Lyve1 (lymphatics) and CD31 (blood vessels) staining. Scale bar = 200µm. The right zoom-in demonstrates a cellular aggregate of $SIRPa^-$ dDC in the lower T cell zone paracortex proximal to the LN medulla. Scale bar = 50µm. **b**, Histo-cytometry gating scheme used to annotate the myeloid cell subsets within the imaging data. **c**, Cellular positions plotted in CytoMAP showing the distinct localization patterns of the indicated immune cell subsets. **d**, The heatmap of SOM clustered, 30µm radius neighborhoods demonstrates different LN regions (top color bar) as defined by the distinct composition of myeloid cells. Regions were also manually annotated (bottom color bar) reflecting the association with B220, CD3 or Lyve1 landmark spots. Annotated gating shown in Fig. S3c. **e**, Positional plot of the LN neighborhoods as color-coded by the region type (panel d - top color bar). **f**, Positional plot of surfaces generated on the manually annotated regions (panel d - bottom color bar). **g**, Violin plot showing the number of cells as a function of distance to the border of the TZ+IFZ annotated region for the representative LN sample. Distances to the left of zero represent cells inside the region;

distances to the right of zero represent cells outside the region. **h**, Plot of the distances of cells to the TZ+IFZ region, in which each dot represents the mean distance of the indicated cell population in an individual LN sample (n=5). **i**, Mean distances of indicated cells to the CMC region. **j**, Mean distances of indicated cells to the B Follicle region. **k**, Correlation plot demonstrating the Pearson correlation coefficients between the number of indicated cells per neighborhood using either all tissue neighborhoods (left) or only the TZ+IFZ region neighborhoods (right). Correlations were averaged over the sample cohort (n=5) from one experiment. For this experiment, an average imaging volume of 0.023 mm^3, and an average of 6,611 myeloid cells, 84,347 spots, and 12,708 neighborhoods were analyzed per sample. Data are representative of at least two independent experiments.

Figure 4. CytoMAP analysis of 3D LNs reveals preferential interactions of DCs with vasculature. a, Representative confocal image of a 500μm thick, Ce3D cleared steady state LN slice. Zoom-in images demonstrate association of Clec9a$^+$ cDC1 cells with CD31$^+$ blood vessels. Main image scale bar = 200μm; zoom-in scale bar = 50μm. **b**, Violin plot comparing the distances of the indicated cells to nearest blood vessels within a representative LN sample. **c**, Mean distances of cell populations to the nearest blood vessel, with each symbol representing an individual LN sample. Circles and squares represent samples from two independent experiments. Cells below the dotted line at 20μm were considered proximal to vasculature. **d**, Percentage of proximal cells for the LN samples shown in c. **e**, Heatmap showing the Pearson correlation coefficients, averaged across all imaged samples, between the number of different cell or landmark object types per 50μm radius neighborhood. Data represent four samples from two independent experiments. For these experiments, an average imaging volume of 0.93 mm^3, and an average of 39,139 myeloid cells, 36,048 blood vessel objects, 98,279 spots, and 133,446 neighborhoods were analyzed per sample.

Figure 5. Individual blood vessel branches in LNs demonstrate selective interactions within specific DC subsets. a, Confocal image demonstrating the CD31-labeled vascular networks in the same representative LN sample as presented in Fig. 4a. Scale bar = 200μm. **b**, Zoom-in of the region in panel a (denoted with a rectangle), demonstrating the centers of CD31$^+$ blood vessel objects (white dots). The circles with yellow dots represent spherical object-centered neighborhoods with a radius of 20μm. Scale bar is 20μm. **c**, Heatmap of the myeloid cell composition for the vessel-centered neighborhoods after SOM clustering. The top color bar shows color-coded regions of neighborhoods. The bottom color bar shows manually annotated regions composed of different DC subsets. **d**, Positional plot of the vascular neighborhoods in a 200μm thick virtual Z section, also color-coded based on the annotations in panel c. Data represent four samples from two independent experiments.

Figure 6. CytoMAP analysis of a murine colorectal tumor sample. a, Multiplex confocal image of a 20μm thick CT26 tumor section isolated 16 days after subcutaneous inoculation and stained with the indicated markers. Zoom in demonstrates the immune cell cuff surrounding the tumor. Main image scale bar = 500μm; zoom-in scale bar = 50μm. **b**, Positional plot of the lymphocyte (top) and myeloid cell (bottom) populations as defined by histo-cytometry gating presented in Fig. S6a. **c**, Heatmap of the normalized immune cell composition of regions defined by SOM clustering of 50μm radius neighborhoods. **d**, Positional plot visualizing the CT26 color-coded regions defined in panel c. **e**, Pseudo-space plot with the number of the indicated cell types per neighborhood after pre-sorting for TAM (sorted to the left) and DCs (sorted to the right) along the pseudo-space linear axis. Neighborhoods were also smoothed, and y-axis normalized to allow qualitative comparison of cell type localization. **f**, Heatmap of the Pearson correlation coefficients of the number of cells per neighborhood across the imaged tumor

sample. For this experiment, an imaging volume of 0.3 mm^3, 34,013 myeloid cells, 22,035 lymphocytes, and 58,608 neighborhoods were analyzed.

Figure 7. CytoMAP analysis of Mtb-infected lung granuloma. a, Multiplex confocal image of a 20μm thick section from a Mtb-infected murine lung sample stained with the indicated antibodies. The left image shows multiple imaged channels overlaid in white to visualize the overall lung structure. Scale bar = 500μm. Zoom in images demonstrate separately acquired regions of interest centered on a representative uninvolved lung area and the Mtb granuloma. Zoom-in scale bar = 100μm. **b**, Positional plots of the immune cell subsets in the uninvolved (top) versus granuloma-containing (bottom) lung areas shown in panel a, with the cell populations defined by the histo-cytometry gating scheme presented in Fig. S7a. **c**, Heatmap of SOM-clustered, 50μm radius neighborhoods demonstrating the distinction between uninvolved lung regions (R1) versus those within the granuloma (R2-R6). **d**, Positional plots of the neighborhoods, color-coded by region defined in panel c, within the uninvolved (top) versus granuloma-containing (bottom) lung areas. **e**, Pseudo-space plots visualizing the number of the indicated cell types per neighborhood within the uninvolved (left) versus granuloma-containing (right) lung areas after sorting for Alv. Macs (sorted to the left) and Mtb^+ cells (sorted to the right) along the pseudo-space axis. Neighborhoods were also smoothed, and y-axis normalized to allow qualitative comparison of cell type localization. **f**, Rotated half-heatmaps demonstrating the Pearson correlation coefficient of the number of cells within the neighborhoods across either the uninvolved lung (left) or the granuloma (right). For the uninvolved lung region, an imaging volume of 0.05 mm^3, 36,194 cells, and 4725 neighborhoods were analyzed. For the granuloma lung region, an imaging volume of 0.07 mm^3, 140,453 cells, and 7,350 neighborhoods were analyzed.

Figure S1. Identification of basic LN architecture with CytoMAP - related to Fig. 2. a, The same LN dataset as presented in Fig. 2a, demonstrating the out-of-plane noise in the CD3 channel within the maximum projection image (left) or a single Z-slice (right). Overview image scale bar = 200μm; zoom-in scale bar = 50μm. **b**, Extended t-SNE analyses for Fig. 2g, demonstrating a color-coded heatmap of the total MFI signal in each neighborhood for the indicated markers. **c**, Interaction map showing the percentage of shared border between the regions, as defined and color-coded in Fig. 2e. The white node represents area external to the tissue. The node size is proportional to the prevalence of that region within the sample (number of neighborhoods per image). Lines connect regions that share borders, with the line thickness being proportional to the percent of the border shared between the regions. **d**, Davies-Bouldin values were used to determine the number of regions presented in Fig. 2d.

Figure S2. Quantifying myeloid cell organization in LNs - related to Fig. 3. a, Two independent representative histo-cytometry plots demonstrating the gating strategy used to annotate cell types and landmark spots in the dataset presented in Fig. 3. **b**, Positional plots of the landmark spots (top left), indicated cell populations, and RDP (bottom right) overlaid on the manually annotated regions, as shown in Fig. 3f.

Figure S3. CytoMAP reveals patterns of myeloid cell organization in LNs - related to Fig. 3. a, Color-coded spatial plots of the neighborhoods, demonstrating the distribution of CytoMAP generated regions across all of the LNs presented in Fig. 3. **b**, Region prevalence plot showing the percentage of the neighborhoods from each sample in each region. **c**, Representative gates on the neighborhoods based on their region number used to manually annotate the regions and define the surfaces shown in Fig. 3f. **d**, Davies-Bouldin values used to determine the number of regions presented in Fig. 3d. **e**, Violin plots of the distances for all cells from each LN. The means of these distances are shown in Fig. 3h-j. TZ+IFZ

distance analysis for LN1 are the same data as presented in Fig. 3g. **f**, Combined analysis for Fig. 3i and 3j. Plot demonstrates the average distance of the indicated cell populations to the B cell follicle versus the CMC, with each dot representing an individual sample. **g**, Heatmaps of the p-values for the Pearson correlation coefficients shown in Fig. 3k. High p-values correspond to correlation coefficients not significantly different from 0. Data represent 5 samples from one independent experiment.

Figure S4. Identification of DC subsets in 3D LNs – related to Fig. 4. a, Histo-cytometry hierarchical gating of the cell populations extracted from two representative samples, one for each experiment, for the data presented in Fig. 4. The classifier is a manually added parameter used to distinguish between different sets of surface objects for gating purposes. **b**, 3D spatial remapping of the cell objects annotated in panel a. **c**, Heatmap of the p-values for the Pearson correlation coefficients presented in Fig. 4e. High p-values correspond to correlation coefficients not significantly different from 0. Data represent four samples from two independent experiments.

Figure S5. Characterization of blood vessel branches in LNs – related to Fig. 5. a, Plot of the Davies-Bouldin values used to determine the number of regions used for SOM clustering presented in Fig. 5c. **b**, Percentage of neighborhoods in each cluster defined in the color bar at the top of Fig. 5c. **c**, Percentage of neighborhoods in each manually defined cluster group from the bottom color bar in Fig. 5c. Data represent four samples from two (circles vs. squares) independent experiments.

Figure S6. Quantitative analysis of tumor immune infiltrate – related to Fig. 6. a, Histo-cytometry plots of the gating strategy used to annotate the cell types for the sample analyzed and presented in Fig. 6. **b**, Davies-Bouldin values used to determine the number of regions in the neighborhood dataset, with the SOM clustering presented in Fig. 6c. Although the absolute minimum of the function indicated presence of up to 18 different regions, 6 regions were used for clustering, as this was relatively similar to the function minimum. **c**, Heatmap of the p-values for the corresponding Pearson correlation coefficients presented in Fig. 6f. High p-values correspond to correlation coefficients not significantly different from 0.

Figure S7. Quantitative analysis of lung Mtb granulomas – related to Fig. 7. a, Histo-cytometry plots showing the gating strategy used to annotate the cell types presented in Fig. 7b. The cell objects extracted from the uninvolved lung image are on the left and the granuloma image are on the right. **b**, The Davies-Bouldin values used to determine the number of regions in the neighborhood dataset, with the SOM clustering presented Fig. 7c. The neighborhoods were clustered into 6 regions based on these values. Since there are two very different regions in this dataset (lung and granuloma) the minimum of the Davies-Bouldin yields only two regions. However, the local minimum at 6 regions reveals both the difference between the lung and granuloma neighborhoods, as well as the different regions within the granuloma. **c**, The color-coded position plot of the regions if 2 regions were used based on the absolute minimum from the Davies-Bouldin function, as presented in panel c. This plot demonstrates two distinct regions, the uninvolved lung (cyan) and the granuloma (yellow). **d**, The p-values for the corresponding Pearson correlation coefficients presented in Fig. 7f. High p-values correspond to correlation coefficients not significantly different from 0.

Video S1. Association of resident cDC1 with LN vasculature – related to Fig. 4. This video shows a 3D visualization of the Ce3D cleared steady state LN (also shown in Fig. 4a), demonstrating close association of Clec9a+ cDC1 with CD31+ LN blood vessels. Clec9a staining is cyan, CD31 staining is red and Lyve1 staining is purple. Clec9a expressing cells are predominantly cDC1 cells.

Video S2. DC subsets associate with distinct LN vascular trees – related to Fig. 5. This video shows a 3D view of the vascular networks (also shown in Fig. 5d), demonstrating large segments of vascular trees preferentially associated with distinct DC populations. Each dot represents a vascular neighborhood. Unassociated vascular neighborhoods – grey; CD207 associated neighborhoods – green; resident cDC1 associated neighborhoods – blue; resident cDC2 associated neighborhoods – red.

Table 1. Key Resources

REAGENT or RESOURCE	SOURCE	IDENTIFIER
Antibody-fluorophore (clone)		
CD3 -BV421; -AF700; -APC-F750; -CF633 [Conjugated in house] (17A2)	BioLegend	Cat# 100228; 100216; 100247; 100202
CD4-CF660 (RM4-5) [Conjugated in house]	BioLegend	Cat# 100506
CD8 (53-6.7)-BV510	BioLegend	Cat# 100752
CD11b (M1/70)	BD	Cat# 55308
CD11c -BV421; -AF647 (N418)	BioLegend	Cat# 117330; 117312
CD11c-eFluor615 (N418)	eBioscience	Cat# 42-0114-82
CD11c-BV480 (HL3)	BD	Cat# 565627
CD31 -BV421; -BV480 (390)	BioLegend; BD	Cat# 102424; 746260
CD31-AF488 (Mec 13.3)	BioLegend	Cat# 102513
CD45.2-BV510 (104)	BioLegend	Cat# 109838
CD64 -PE; -CF660 [Conjugated in house] (X54-5/7.1)	BioLegend	Cat# 139304; 139302
CD169-CF514 (3D6.112) [Conjugated in house]	BioLegend	Cat# 142402
CD207 -AF488; -AF546 (929F3.01)	Fisher Scientific	Cat# DDX0362A488; DDX0362A546
CD301b-CF660 (URA1) [Conjugated in house]	BioLegend	Cat# 146802
B220 -biotin; -BV510; -AF700; -CF750 [Conjugated in house] (RA3-6B2)	BioLegend	Cat# 103204; 103247; 103232; 103202
B220 (RA3-6B2)-DY405LS	Novus Biologicals	Discontinued
CXCR3-PE (CXCR3-173)	Fisher Scientific	Cat# 12-1831-82
Foxp3-eF570 (FJK-16s)	eBioscience	Cat# 41-5773-82
IFNg-PE (XMG1.2)	BioLegend	Cat# 505807
iNOS (C-11)-AF405	Santa Cruz	Cat# sc-7271
IRF4 -CF514; -CF594 (IRF4.3E4) [Conjugated in house]	BioLegend	Cat# 646402
Jojo1	Invitrogen	Discontinued
Ki67-AF700 (B56)	BD	Cat# 561277
Lyve1 -biotin; -eFluor570 (ALY7)	eBioscience	Cat# 13-0443-82; 41-0443-82
MHC-II -AF700; -Dy395xl (M5/114.15.2)	BioLegend	Cat# 107622; 107602
Mtb (rabbit polyclonal)	Abcam	Cat# Ab905
PCREB-AF488 (87G3)	Cell Signaling	Cat# 9187S
pS6 (2F9)-AF488	Cell Signaling	Cat# 48554
SIRPα -BV421; -CF594 [Conjugated in house] (P84)	BD; Biolegend	Cat# 624124; 14401
TCF1-PacBlue (C63D9)	Cell Signaling	Cat# 9066S
anti-rabbit-AF750	Invitrogen	Cat# A-21039
SA-AF750	Invitrogen	Cat# S21384
SA-ATTO490LS	ATTO-TEC	Cat# AD490LS-61
anti-GFP-AF488	Invitrogen	Cat# A-21311

Chemicals, Peptides, and Recombinant Proteins		
Tissue-Tek O.C.T. Compound	Electron Microscopy Sciences	Cat# 62550-01
BD Cytofix fixation buffer	BD Biosciences	Cat# 554655
PBS (pH 7.4)	Caisson Labs	Cat# PBL06-6X500ML
Triton-X-100	Sigma-Aldrich	Cat# T-9284
Bovine Serum Albumin	Sigma-Aldrich	Cat# A9576-50ML
Normal Mouse Serum	Jackson Laboratories	Cat# 015-000-120
Tris buffer (1 M dilute to 0.1M)	Fisher Scientific	BP1756500
Mix-n-Stain CF Dye Antibody Labeling Kits	Biotium	Cat# 92433-92339
N-methylacetamide	Sigma-Aldrich	Cat# M26305
Histodenz	Sigma-Aldrich	Cat# D2158
1-Thioglycerol	Sigma-Aldrich	Cat# M1753
High-vacuum grease	VWR	Cat# DOWC1597418
Agarose	Fisher Scientific	Cat# 16500500
Immersion Oil, type F	Fisher Scientific	Cat# NC0586121
EndoFit Ovalbumin 100mg	Invivogen	Cat# vac-nova-100
Alhydrogel adjuvant 2% , 250mL	Invivogen	Cat# vac-alu-250
Sucrose, ultrapure DNAse- and RNAse-free	VWR	Cat# 97061-432
Deposited Data		
Software		
CytoMAP	This Manuscript	https://gitlab.com/gernerlab/cytomap
Imaris extensions	This Manuscript	https://gitlab.com/gernerlab/imarisxt_histocytometry
Imaris	Bitplane	https://imaris.oxinst.com/
LASX	Leica Microsystems	https://www.leica-microsystems.com/products/microscope-software/p/leica-las-x-ls/
FlowJo	FlowJo, LLC	https://www.flowjo.com/
Prism	GraphPad Software	https://www.graphpad.com/scientific-software/prism/
MATLAB	The MathWorks, Inc.	https://www.mathworks.com/products/matlab.html?s_tid=hp_products_matlab
Other		
UltraComp eBeads Compensation Beads	Fisher Scientific	Cat # 01-2222-42

PAP pen	Vector Laboratories	Cat# H-4000

Table 2 Channel Arithmetic

Channel name/Sample	Description	Equation
Fi. 2		
All Cell Composite	CD3 + 0.5*CD45.2 + MHC-II	(ch1 .* 0.5) + (ch3.* 0.5) + ch5
Fig. 3		
clean-CD31	corrected spillover from CD11c	(ch7-ch6).*(ch7>ch6)
clean-SIRPa	corrected spillover from CD31	(ch2-ch7).*(ch2>ch7)
clean-CD169	exclude CD207+ subtract CD31	(ch4-ch13).*(ch4>ch13).*(ch3<70)
clean-CD11c	corrected spillover from CD31	(ch6-ch13).*(ch6>ch13)
clean-MHC-II	exclude B220	(ch8-ch11).*(ch8>ch11)
Composite Myeloid	clean-SIRPa + CD207 + clean-CD169 + clean-CD11c + clean-MHC-II + Clec9a	(ch14.*0.75) + (ch3.*0.75) + (ch15.*0.5) + (ch16.*0.9) + (ch17.*0.75) + (ch9 .* 0.75 .*(ch9>50))
Fig. 4 Experiment #1		
Clean CD31	CD31-0.1*Lyvel	(ch1-0.1.*ch8).*(ch1>0.1.*ch8)
Composite Myeloid	CD11c + Clec9a + CD207 + CD169 + SIRPa + CD301b + MHC2	ch2+ch4+ch5+ch6+ch7+ch9+(ch10.*4)
Fig. 4 Experiment #2		
Composite Myeloid	CD169 + 2*SIRPa + 2.5*MHC-II(B220<55) + Clec9a+CD207 + 1.5*CD11c - B220 - CD3 + min("")	((1.5.*ch1.*(ch1>5) + 3.8.*ch4.*(ch4>5) + 2.5.*ch6.*(ch6>5).*(ch5<40) +2.*ch7.*(ch7>5) + ch9.*(ch9>5) + 2.*ch10.*(ch10>5)-0.5.*ch3-0.5.*ch5) +min(min((1.5.*ch1.*(ch1>5) + 3.8.*ch4.*(ch4>5) + 2.5.*ch6.*(ch6>5).*(ch5<40) +2.*ch7.*(ch7>5) + ch9.*(ch9>5) + 2.*ch10.*(ch10>5)-0.5.*ch3-0.5.*ch5)))))./2
Fig. 6		
Composite Lymphocyte	CD3+2*B220	ch10+(2.*ch8)
Composite Myeloid	CD11c+MHC-II+1.3*CD64	ch2+ch4+(1.3.*ch9)
Fig. 7		
Composite Surface Markers	[(CD11c>14)/175 + (CD11b>10.5)/160 + (B220>15)/130 + (CD3>30)/170 + (MHC-II>20)/165]*150	(ch2.*(ch2>14)./175 + ch3.*(ch3>10.5)./160 + ch4.*(ch4>15)./130 + ch5.*(ch5>30)./170 + ch11.*(ch11>20)./165).*150
Nuclei	Jojo1 – Composite Surface Markers	ch8 - ch13

Table 3. Surface creation parameters

Surface Spots Name	Source Channel	Smoothing: Surface Detail (µm)	Background Subtraction: Diameter of Largest sphere	Absolute Intensity Threshold	Split Touching Objects: Split seed diameter (µm)	Quality Threshold	Voxel Number Threshold	Sphericity Threshold	Diameter (Spots)
Fig. 2									
Surface_1	All Cell Composite	20		8					
Surface_2	Inverted Ch	0.655		107	3.28	8.28	10-2781	0.583	
Fig. 3									
Myeloid Surfaces	Composite Myeloid	0.758	25	7-22 (Sample Dependent)	7.5-10 (Sample Dependent)	4.5	300		
All Spots	B220					13.1			3
Fig. 4 Experiment #1									
Myeloid Surfaces	Composite Myeloid	1.5	12	20	12	10	50		
CD31 Surfaces	Clean CD31	2.5	15	2.25	4	3.5	150		
Lyve1 Spots	Lyve1		true			2			5
B220 Spots	B220		true LN1 (false LN2)			1.5 LN1 (7.5 LN2)			5
Fig. 4 Experiment #2									
Myeloid Surfaces	Composite Myeloid	0.8	11	40	10	6	50		
CD31	CD31	2	5	2	4	2.5	50		

Surfaces									
Lyve1 Spots	Lyve1		false			20			5
B220 Spots	B220		false			40			5
Fig. 6									
Myeloid Surfaces	Composite Myeloid	0.6	11	20	11	5	50-7103		
Lymphocyte Surfaces	Composite Lymphocyte	0.6	10	9	6	2.5	50		
Fig. 7									
All Cells	Nuclei	0.63	10	18.5	3.16	6.08	10		

Table 4. Pseudo-space input parameters

Fig. 2f Data Preparation: Neighborhood Composition		
Cell Type	Weight	Smoothing
B cells	-1	500
T Cells	1	500
DCs	0.2	500
Fig. 6e Data Preparation: Number of cells per Neighborhood		
Type	Weight	Smoothing
B cells	1	5000
Teff	0	5000
Treg	5	5000
TAM	-2	5000
DCs	0	5000
aMACs.	1	5000
SIRPα^{DIM}MHC-II+	-1	5000
Fig. 7e Data Preparation: Number of cells per Neighborhood		
B Cells	1	1000
Alv. Macs	-50	1000
CD11b+	0	500
DCs	0	1000
Mtb+ Cells	100	100
T Cells CD4-	1	1000
T Cells CD4+	1	1000

Table 5. Antibody staining panels and Microscope Settings

Ch	Antibody	Flurophore
Fig. 2		
1	CD3	421
2	TCF1	PacBlue
3	CD45.2 (OT-II)	510
4	CXCR3	PE
5	MHC-II	594
6	Ki67	700
7	B220	CF750
8	anti-GFP	AF488
9	CD11c	647
Fig. 3		
1	CD64	PE
2	SIRPα	594
3	CD207	488
4	CD169	514
5	Lyve1	490LS
6	CD11c	421
7	CD31	480
8	MHC-II	395xl
9	Clec9a	633
10	CD301b	660
11	B220	700
12	CD3	APC-f750
Fig. 4 Experiment #1		

1	CD31	BV421
2	CD11c	BV480
3	B220	Dy405ls
4	Clec9a	CF633
5	CD207	AF488
6	CD169	CF514
7	SIRPa	CF594
8	Lyve1	eFluor570
9	CD301b	CF660
10	MHC-II	AF700
Fig. 4 Experiment #2		
1	CD169	CF514
2	CD3	AF700
3	Lyve1-biotin	SA-CF750
4	SIRPa	BV421
5	B220	BV510
6	MHC-II	DY395XL
7	Clec9a	CF633
8	CD31	AF488
9	CD207	AF546
10	CD11c	eFluor615
Fig. 6		
1	SIRPa	BV421
2	CD11c	BV480
3	CD8	BV510
4	MHC-II	Dy396XL
5	Clec9a	αsheep-CF633
6	PCREB	AF488
7	IRF4	CF514
8	B220	SA-490ls
9	CD64	CF660c
10	CD3	AF700
11	PD1	αgoat-CF750
12	Foxp3	eF570
13	PD-L1	CF594
Fig. 7		
1	iNOS	AF405
2	CD11c	BV480
3	CD11b	
4	B220	405ls
5	CD3	CF633
6	pS6	AF488
7	IFNg	PE
8	Jojo1	
9	IRF4	CF594
10	CD4	CF660
11	MHC-II	AF700
12	Mtb	CF750

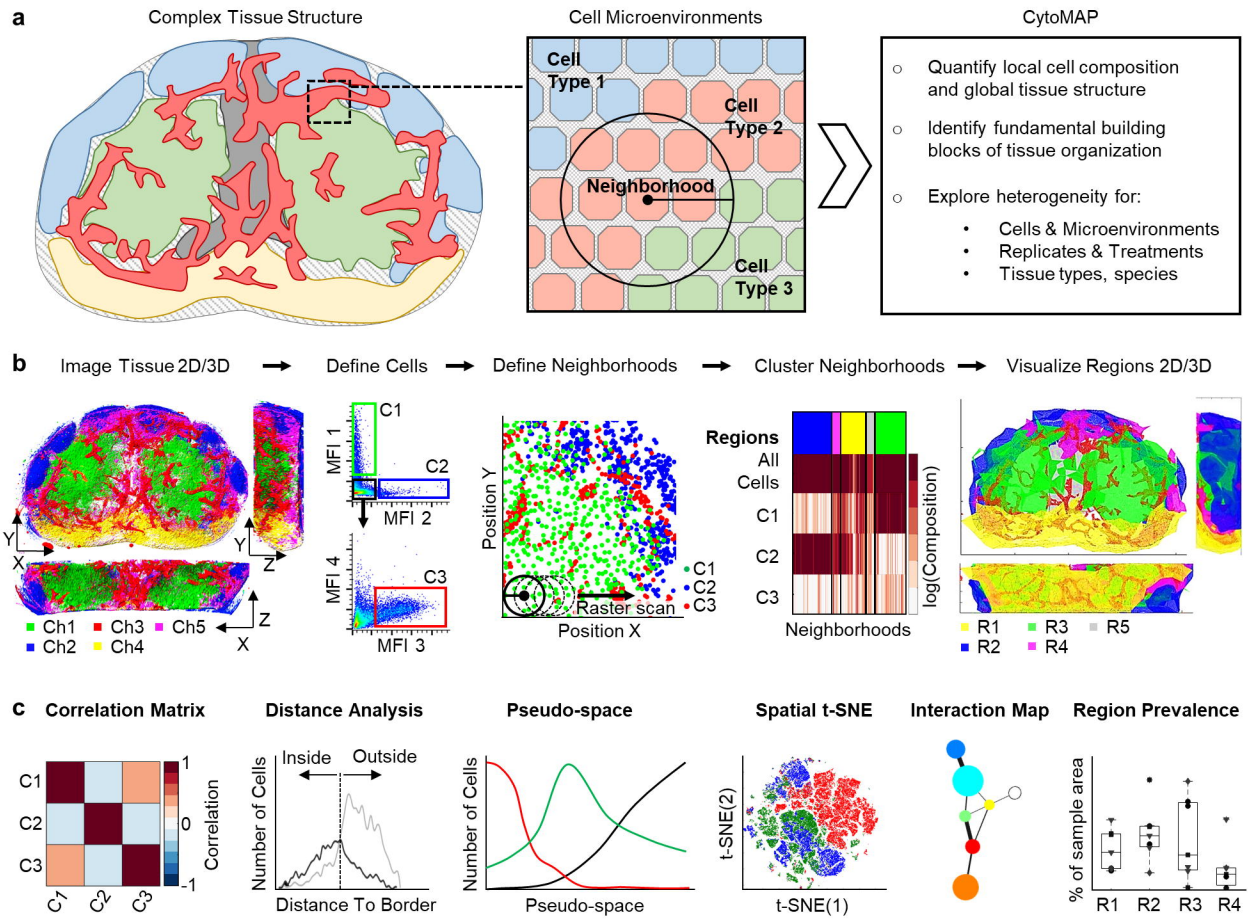
a
Complex Tissue Structure
Cell Microenvironments
Cell Type 1
Cell Type 2
Neighborhood
Cell Type 3
CytoMAP
Quantify local cell composition and global tissue structure
Identify fundamental building blocks of tissue organization
Explore heterogeneity for:
Cells & Microenvironments
Replicates & Treatments
Tissue types, species
b
Image Tissue 2D/3D
Define Cells
Define Neighborhoods
Cluster Neighborhoods
Visualize Regions 2D/3D
Ch1 Ch3 Ch5
Ch2 Ch4
MFI 1
MFI 2
MFI 4
MFI 3
C1
C2
C3
Position Y
Position X
Raster scan
Regions
All Cells
log(Composition)
Neighborhoods
R1 R3 R5
R2 R4
c
Correlation Matrix
Distance Analysis
Pseudo-space
Spatial t-SNE
Interaction Map
Region Prevalence
Correlation
Inside
Outside
Number of Cells
Distance To Border
Pseudo-space
t-SNE(2)
t-SNE(1)
% of sample area
R1 R2 R3 R4

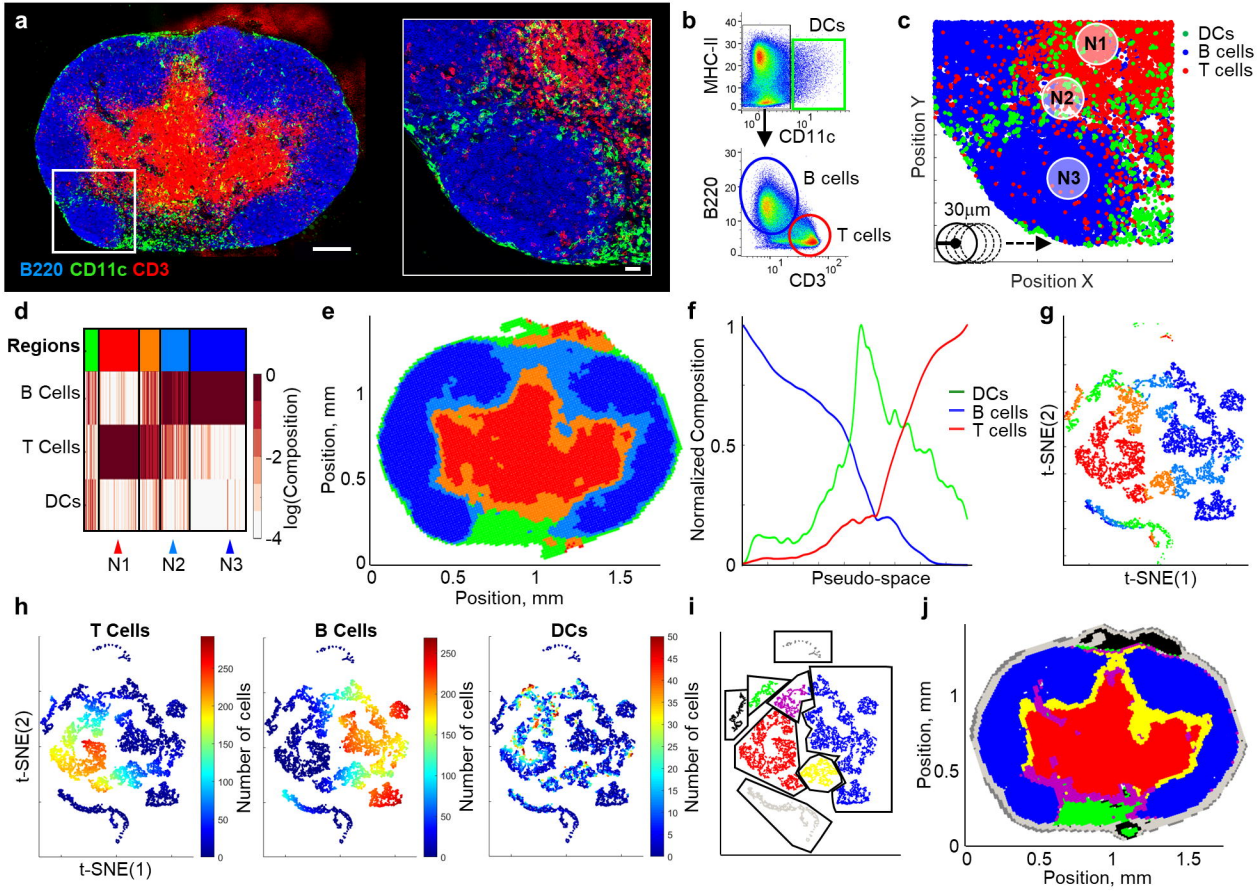
a
B220 CD11c CD3
b
DCs
MHC-II
CD11c
B220
B cells
T cells
CD3
c
N1
N2
N3
DCs
B cells
T cells
Position Y
30μm
Position X
d
Regions
B Cells
T Cells
DCs
N1
N2
N3
log(Composition)
e
Position, mm
f
Normalized Composition
DCs
B cells
T cells
Pseudo-space
g
t-SNE(2)
t-SNE(1)
h
T Cells
B Cells
DCs
t-SNE(2)
t-SNE(1)
Number of cells
i
j
Position, mm

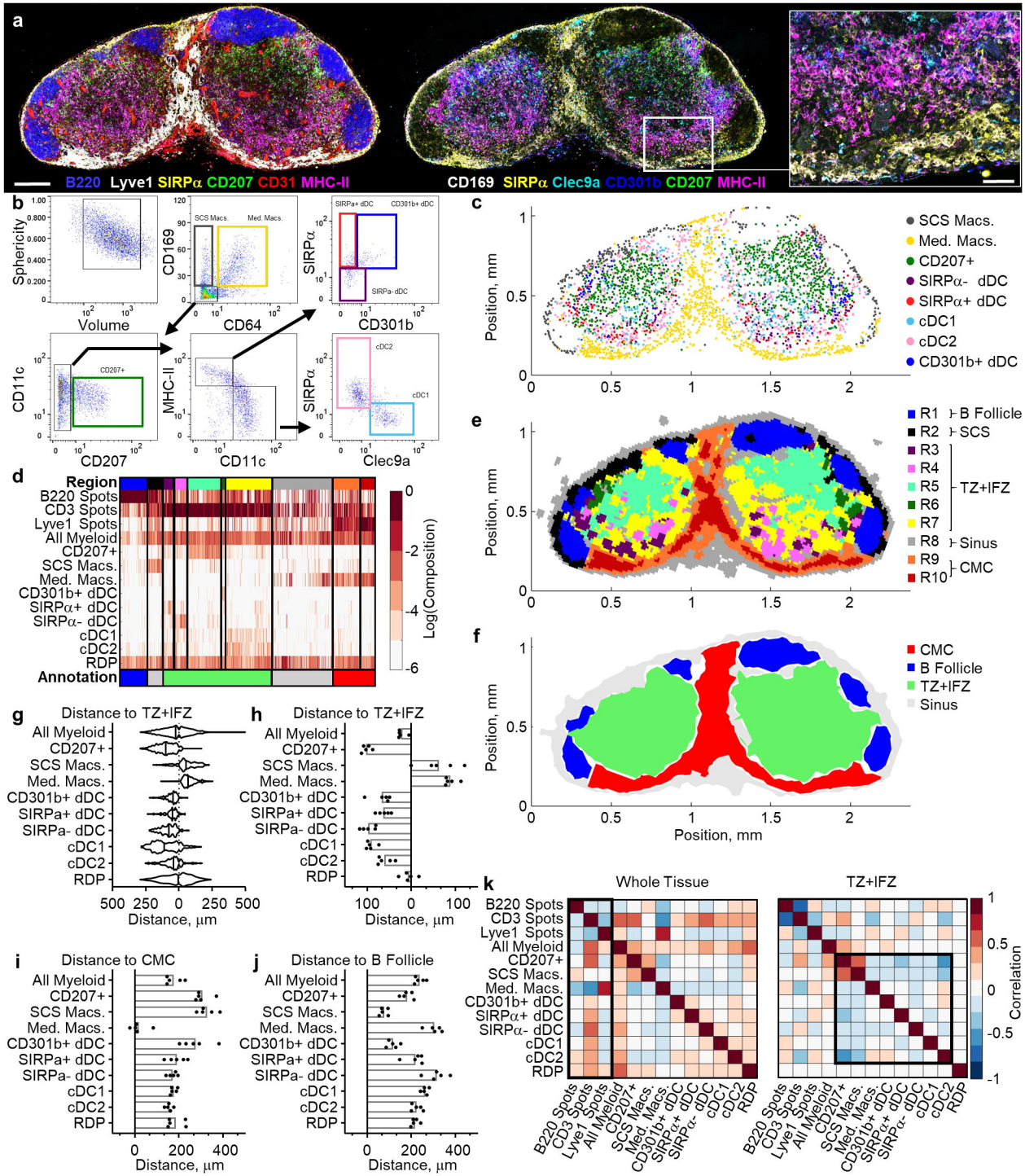
a
B220 Lyve1 SIRPα CD207 CD31 MHC-II
CD169 SIRPα Clec9a CD301b CD207 MHC-II
b
Sphericity
Volume
CD169
CD64
SCS Macs.
Med. Macs.
SIRPα
CD301b
SIRPa+ dDC
CD301b+ dDC
SIRPa- dDC
CD11c
CD207
CD207+
MHC-II
CD11c
SIRPα
Clec9a
cDC2
cDC1
c
Position, mm
SCS Macs.
Med. Macs.
CD207+
SIRPα- dDC
SIRPα+ dDC
cDC1
cDC2
CD301b+ dDC
e
R1
R2
R3
R4
R5
R6
R7
R8
R9
R10
B Follicle
SCS
TZ+IFZ
Sinus
CMC
f
CMC
B Follicle
TZ+IFZ
Sinus
d
Region
B220 Spots
CD3 Spots
Lyve1 Spots
All Myeloid
CD207+
SCS Macs.
Med. Macs.
CD301b+ dDC
SIRPα+ dDC
SIRPα- dDC
cDC1
cDC2
RDP
Annotation
Log(Composition)
g
Distance to TZ+IFZ
Distance, µm
h
Distance to TZ+IFZ
Distance, µm
i
Distance to CMC
Distance, µm
j
Distance to B Follicle
Distance, µm
k
Whole Tissue
TZ+IFZ
Correlation

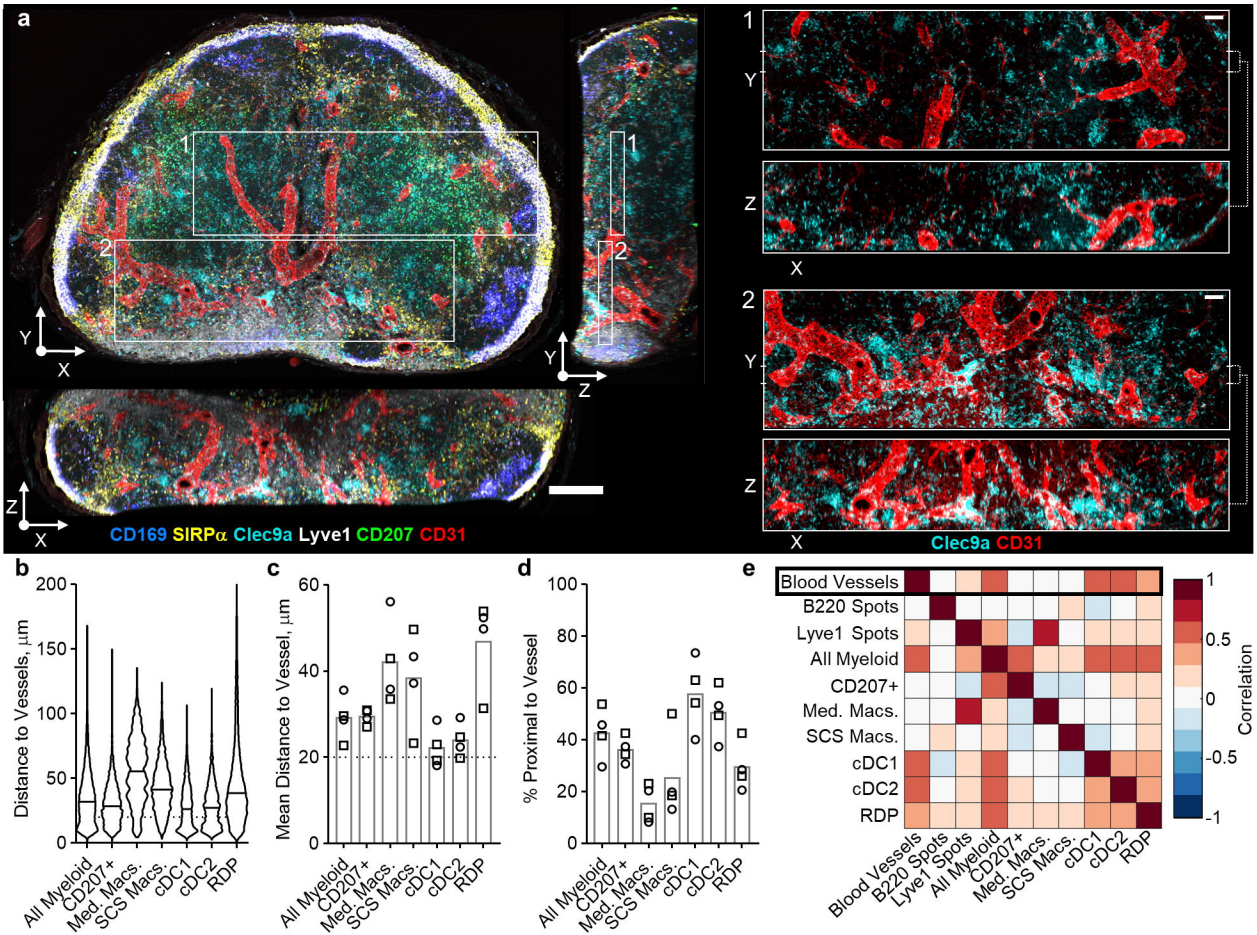
a
1
2
Y
X
Z
CD169 SIRPα Clec9a Lyve1 CD207 CD31
Clec9a CD31
b
Distance to Vessels, µm
c
Mean Distance to Vessel, µm
d
% Proximal to Vessel
All Myeloid
CD207+
Med. Macs.
SCS Macs.
cDC1
cDC2
RDP
e
Blood Vessels
B220 Spots
Lyve1 Spots
Correlation

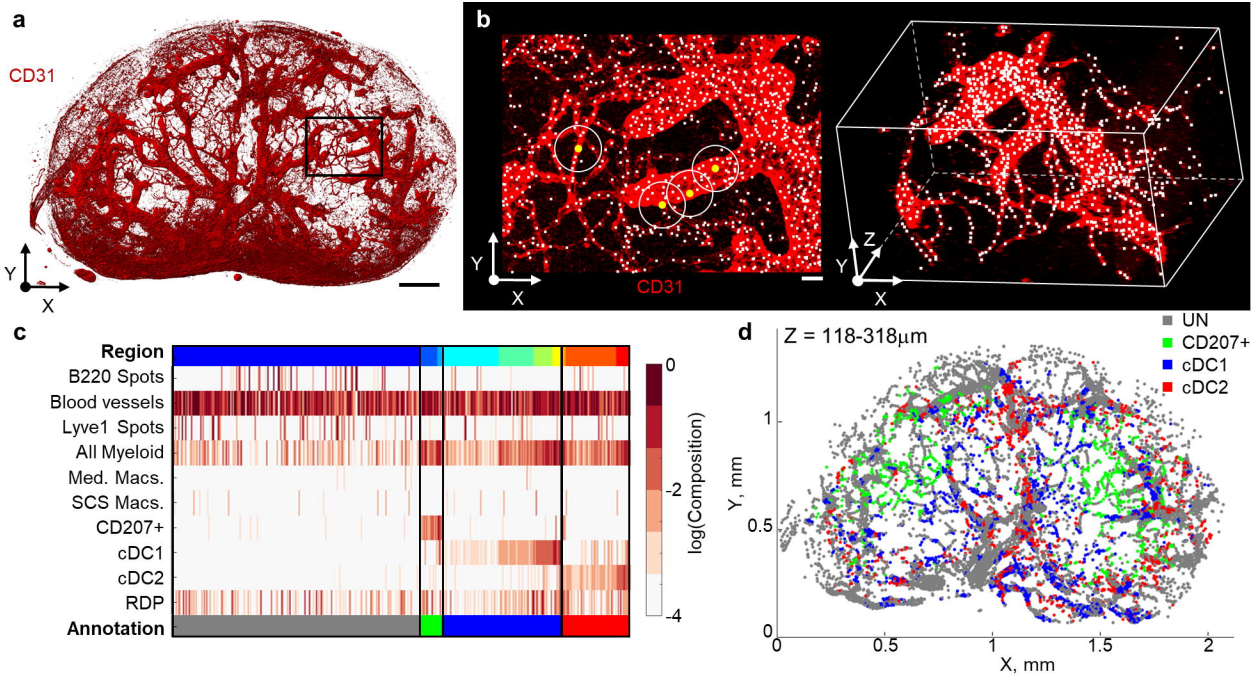
a
CD31
Y
X
b
Y
X
CD31
Z
Y
X
c
Region
B220 Spots
Blood vessels
Lyve1 Spots
All Myeloid
Med. Macs.
SCS Macs.
CD207+
cDC1
cDC2
RDP
Annotation
0
-2
-4
log(Composition)
d
Z = 118-318μm
UN
CD207+
cDC1
cDC2
Y, mm
X, mm
0
0.5
1
1.5
2

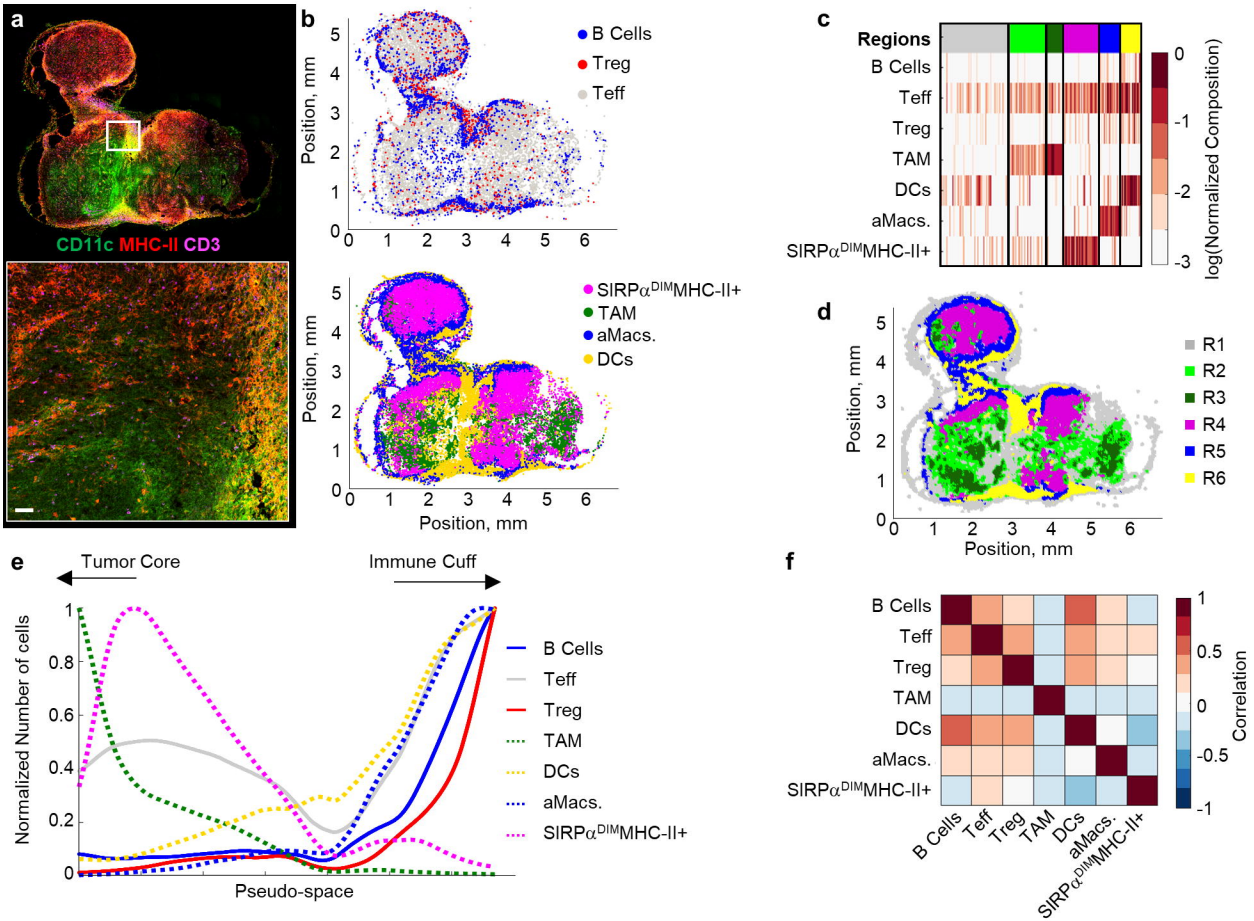
a
CD11c MHC-II CD3
b
B Cells
Treg
Teff
SIRPα^DIM MHC-II+
TAM
aMacs.
DCs
Position, mm
c
Regions
B Cells
Teff
Treg
TAM
DCs
aMacs.
SIRPα^DIM MHC-II+
log(Normalized Composition)
d
R1
R2
R3
R4
R5
R6
Position, mm
e
Tumor Core
Immune Cuff
Normalized Number of cells
Pseudo-space
f
Correlation

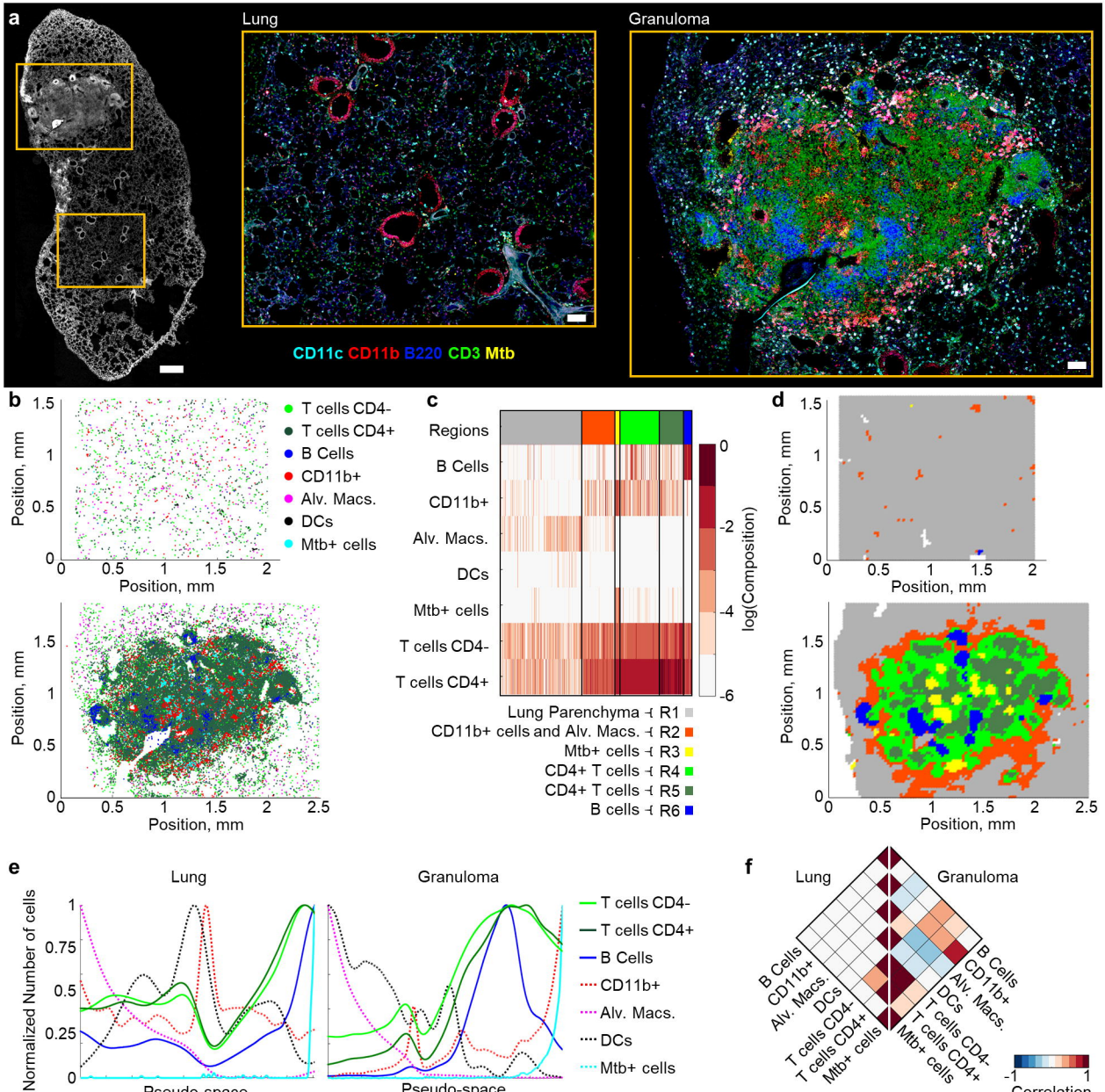
a
Lung
Granuloma
CD11c CD11b B220 CD3 Mtb
b
Position, mm
T cells CD4-
T cells CD4+
B Cells
CD11b+
Alv. Macs.
DCs
Mtb+ cells
c
Regions
B Cells
CD11b+
Alv. Macs.
DCs
Mtb+ cells
T cells CD4-
T cells CD4+
log(Composition)
Lung Parenchyma R1
CD11b+ cells and Alv. Macs. R2
Mtb+ cells R3
CD4+ T cells R4
CD4+ T cells R5
B cells R6
d
Position, mm
e
Lung
Granuloma
Normalized Number of cells
Pseudo-space
f
Lung
Granuloma
Correlation